Please find the published version at:
https://doi.org/10.1016/j.ijheatmasstransfer.2021.122315

The droplets and film behaviors in supersonic separator by using three-field two-fluid model with heterogenous condensation

Hongbing Ding[1,*], Chunqian Sun[1], Chuang Wen[2], Zhenxin Liang[1]

[1]Tianjin Key Laboratory of Process Measurement and Control, School of Electrical and Information Engineering, Tianjin University, Tianjin 300072, China

[2]College of Engineering, Mathematics and Physical Sciences, University of Exeter, Exeter EX4 4QF, United Kingdom

*Corresponding author: Hongbing Ding, Email: hbding@tju.edu.cn

Abstract:

Supersonic separator is a kind of natural gas dehydration device with great potential, but its internal mass and heat transfer process has not been fully studied. In this study, a novel three-field two-fluid model described by Eulerian-Eulerian approach for supersonic separator considering the heat and mass transfer between gas, liquid droplets, and liquid film was developed and validated. The interphase slip, latent heat, film heat flux, and film phase change rate were studied. It revealed that the maximum centrifugal slip velocity of droplets can reach 24.9 m s^{-1}. The maximum latent heat is 5.3×10^{8} J m^{-3} from droplets to gas phase during condensation, and the minimum latent heat is -3.4×10^{8} J m^{-3} during evaporation. The thickness of swirling liquid film at wet gas outlet is 21 μm, 47 μm, 74 μm and 89 μm, respectively. The liquid film temperature decreases to a minimum 304.1 K due to droplets deposition, where the maximum heat flux is 0.74 MW m^{-2}. Besides, the frequency and velocity of the interfacial wave of liquid film were obtained by using the cross-correlation algorithm, and their maximum values was 11.07 Hz and 1.49 m s^{-1}, respectively. In addition, for achieving higher dehydration efficiency, the optimal value of effective density of foreign droplets should be 0.01 kg m^{-3}. The maximum separation efficiency and dew point depression of separator A are 85.11% and 40.32°C, respectively. The model without considering the liquid film over-predicts the separation efficiency.

Keywords: Three-field two-fluid model; Heterogenous condensation; Supersonic flows; Liquid film; Interfacial wave.

Nomenclature			
a_c	centrifugal acceleration, m s^{-2}	T_w	wall temperature, °C
a	heat transfer coefficient, W m^{-2} K^{-1}	$\vec{u}$	velocity vector, m s^{-1}
C_c	Cunningham slip correction factor, -	$\vec{U}_d$	momentum source term of film, Pa
C_D	drag coefficient, -	u_w	interfacial wave velocity, m s^{-1}
C_{phase}	phase change constant, -	Vs	slip velocity, m s^{-1}
d	cell-center-to-wall distance, m	x	Cartesian coordinate, mm
D_T	subcooling, °C	x_1, x_2	film collecting point 1 and 2, mm

E	total energy, J kg^{-1}	x_l	transit distance, mm
f	collision frequency, Hz	y_1, y_2	fluctuation of film thickness at x_1, x_2, μm
f_w	interfacial wave frequency, Hz	Y_i	mass fraction of species, -
$\vec{F}_D$	drag force, kg m^{-2} s^{-2}	*Greek*	
$\vec{g}$	gravity vector, m^{-1} s^{-2}		
$\vec{g}_\tau$	gravity component parallel to film, m^{-1} s^{-2}	α	volume fraction, -
h_f	enthalpy of film, J kg^{-1}	ρ	density, kg m^{-3}
h_i	enthalpy of specie, J kg^{-1}	$\bar{\bar{\tau}}$	effective stress tensor, Pa
h_{lg}	latent heat of water vapor, J kg^{-1}	τ_0	transit time, s
J	homogeneous nucleation rate, m^{-3} s^{-1}	$\vec{\tau}_{fs}$	viscous shear stress on gas-film interfaces, Pa
$\vec{j}$	diffusion flux, kg s^{-1} m^{-2}	λ	thermal conductivity, W m^{-1} K^{-1}
k_B	Boltzmann's constant. 1.38×10^{-23} J K^{-1}	μ	molecular dynamic viscosity, Pa s
Kn	Knudsen number, -	δ	film thickness, μm
$\dot{m}$	droplet mass changing rate, kg m^{-3} s^{-1}	υ	water molecule volume, m^3
$\dot{m}_c$	mass source term due to collision and coalescence, kg m^{-3} s^{-1}	σ	liquid surface tension, N m^{-1}
$\dot{m}_d$	deposition rate, kg m^{-2} s^{-1}	Φ	relative humidity, $p_v/p_s(T_g)$×100%
m_{evap}	film evaporation rate, kg s^{-1}	χ	mole fraction of water vapor, -
m_m	water molecular mass, 2.99×10^{-26} kg	η_v	water removal rate (i.e., separation efficiency), %
$\dot{m}_{phase}$	film phase change rate, kg m^{-2} s^{-1}	ΔT_d	dew point depression, °C
M	mass diffusivity of water vapor, m^2 s^{-1}	*Subscripts*	
n	volumetric concentrations of droplet, m^{-3}		
N_c	source term due to collision, m^{-3} s^{-1}	*	stagnation condition
p	pressure, Pa	a, r, t	axial, radial, tangential
q_w	surface heat flux, kW m^{-2}	eff	effective
Q	droplet flow rate, ml min^{-1}	f	liquid film
r	droplet radii, μm	g	gas
r_c	critical radii of homogenous nucleus, μm	het/hom	hetero- and homogeneous
$R_{12}(\tau)$	cross-correlation function, -	i	species
Re_p	relative Reynolds number, -	l	liquid

R_v	specific gas constant, J $kg^{-1}·K^{-1}$	max	maximum
S	swirl strength, -	s	saturation
S_i	mass source term of species, kg m^{-3} s^{-1}	tu	turbulent
S_s	water vapor supersaturation, -	v	water vapor
t	time, s	w	interfacial wave
T	temperature, °C	*Superscripts*	
T_d	dew point temperature, °C		
T_m	film half depth temperature, °C	dry, wet	dry and wet gas outlets
T_s	film surface temperature, °C	in, out	inlet, outlet
T_r	droplet surface temperature, °C		

1 Introduction

As a kind of clean energy, natural gas contains almost no sulfur, dust and other harmful substances, and produces less carbon dioxide when burned than other fossil fuels, so it can reduce carbon emissions and environmental pollution [1]. Natural gas contains saturated water that leads to many hazards. For example, the formation of hydrates during transportation causes pipelines and valves to block [2], moreover, the action of water with carbon dioxide, hydrogen sulfide, and other acid gases will corrode pipelines and equipment [3]. Therefore, natural gas dehydration processing is very important. The supersonic separator is a new type of natural gas dehydration device. Because of its simple structure, small size, and no rotating parts [4], it is more suitable for offshore natural gas processing [5], which has attracted the attention of many scholars in recent years.

The two main processes of the supersonic separator are condensation and swirl separation [6]. The components producing these two processes are the supersonic nozzle and the swirl generator, respectively. As shown in Fig. 1, due to the complex three-field (gas, droplets, and liquid film) two-fluid (gas and liquid) [33] characteristics in the supersonic separator, including complex phase changes (condensation and evaporation), interphase slip, liquid film, swirl flow, and shockwave phenomenon [8], even though many scholars have performed flow field analysis and structural optimization of supersonic separators, there are still many problems that need to be fully studied, especially the droplets and liquid film behaviors in supersonic separators.

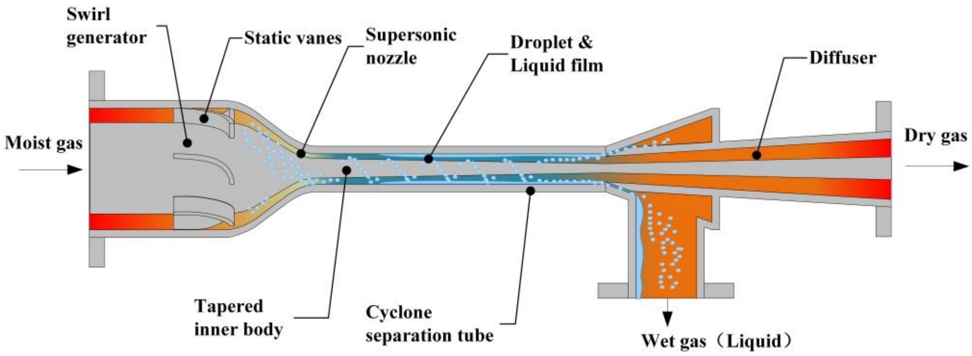

Fig. 1 Three-field characteristics of gas, droplets, and liquid film in supersonic separator.

There are three main methods to study the supersonic separator: theory, experiment and simulation. Because the use of natural gas for experiments is expensive and dangerous, air is often used as feed carrier gas in low pressure experiments instead of natural gas [9]-[10], which has little effect on the experimental results. The experimental results of Ma et al. [11] showed that the injection of foreign droplets caused heterogeneous condensation, which effectively improved the separation efficiency. Cao et al. [12] conducted an experimental study on a new type of supersonic separator with ellipsoidal center body to evaluate dehydration performance. The results showed that the maximum dew point depression could be 34.9℃ at 20.6% pressure recovery coefficient. Wang et al. [13] carried out an experimental study on a novel supersonic separator with reflux channel. The results showed that the cylindrical drainage structure can reduce the interaction between shock wave and boundary layer, thereby improving separation performance. The process simulations in Aspen HYSYS were carried out by de Oliveira Arinelli et al. [14]-[15] to study the offshore natural gas processing with high CO_2 content based on supersonic separators. Simultaneously, the computational fluid dynamics can simulate the distribution characteristics of the flow field by establishing an appropriate numerical model. Therefore, many scholars have established different numerical models for supersonic separators.

The first commonly used model is a two-fluid model based on the Discrete Particle Method (DPM), namely Eulerian-Lagrangian approach, which can track the trajectory of droplets. Wen et al. [16] established a numerical model based on RNG k-ε turbulence model and Discrete Particle Method (DPM) to calculate the flow field and droplet trajectory in a supersonic separator. The results showed that when the separation section length is 10 times the throat diameter, the separation efficiency can reach 95%. The particle behaviors in a supersonic separator with strong swirling flow were modeled by Yang et al. [17] The results showed that majority of the particles were separated by centrifugation to the wall or directly into the moisture outlet, moreover, the separation efficiency reached 80% at the droplet size of 1.5 μm. Liu et al. [18] established compressible Navier-Stokes equations coupled DPM to predict the separation efficiency. The results showed that increasing the droplet size within a certain range improved the separation efficiency.

Jiang et al. [19] analyzed the effect of droplet size and inlet velocity on separation efficiency. The results showed that the droplets were effectively separated when the droplets size was about 1 μm. A numerical model taking into account the actual droplet size distribution was established by Shooshtari et al. [20] to simulate a more realistic condensation droplet trajectory. However, the existing DPM-based two-fluid model does not consider the condensation and evaporation of droplets in the supersonic separator, thus, which has great limitations.

Another commonly used model is the Eulerian two-fluid model, namely Eulerian-Eulerian approach, which takes into account the condensation and evaporation processes. Dykas et al. [21] used Eulerian-Eulerian approach to simulate the homogeneous condensing flow in low- and high-pressure supersonic nozzle, and studied the performance of the numerical algorithm in terms of gas and liquid properties. Patel et al. [22] using Eulerian-Eulerian model combining with modified turbulence model investigated the irreversible heat and mass transfer losses in the condensation process in in nozzle and turbine cascade. White et al. [23] and Ding et al. [24] performed numerical simulation to obtain the distribution of polydisperse droplets of condensing flow. Edathol et al. [25] using Eulerian-Eulerian models predicted the homogeneous condensing flow in a supersonic nozzle. It was found that more experimental validations under different geometric and boundary conditions were needed to validate the effectiveness of the non-equilibrium condensation model. Abadi et al. [26] established a Eulerian-Eulerian model for solving the wet steam flow in the high-pressure nozzle. The results showed that the decreased superheat level makes the nucleation process happen earlier. Wen et al. [27]-[28] developed a Eulerian two-fluid model to study the flow field structure where non-equilibrium condensation and shock coexisted in a supersonic separator, and analyzed the influence of swirl strength on the condensation process. Liu et al. [2] analyzed the influence of the pressure recovery process on the condensation and evaporation of droplets. The results showed that the interaction of shock waves and boundary layers would reduce the liquefaction efficiency. Under actual operating conditions, saturated natural gas contains foreign liquid droplets before entering the dehydration equipment, thus, it is actually heterogeneous condensation in the supersonic separator. Niknam et al. [29] conducted heterogeneous condensation experiments to study the dehydration efficiency of a supersonic separator, moreover, who established a two-phase heat and mass transfer model in a 2D asymmetric domain to predict the dehydration efficiency. Shooshtari et al. [30] assumed that certain rates of salt particles were injected into the supersonic separator, thereby a Eulerian multi-fluid model considering homogeneous/heterogeneous condensation was established. The results showed that the particle injection rate had a profound effect on the separation efficiency. However, the above Eulerian two-fluid models do not consider interphase slip and droplet drag. In our previous research, Ding et al. [8] established a homogeneous/heterogeneous condensation model considering interphase slip and droplet drag, which was verified to have high calculation accuracy and was used to obtain droplet behavior characteristics.

However, the above numerical models only model the two fields (gas and droplets), ignoring the formation of liquid film. Recently, no scholar has established a three-field (gas, droplets, and liquid film) two-fluid model considering liquid film for supersonic separator.

Eulerian-Lagrangian coupled Eulerian wall film model and Eulerian-Eulerian coupled Eulerian wall film model are applied to the modeling of the annular-mist flow. Deng et al. [31] used Eulerian-Lagrangian coupled Eulerian wall film model to simulate the heat and mass exchange between gas, liquid droplets and liquid film in an axial flow cyclone. The results showed that under the centrifugal action of the guide vanes, the droplets moved to the wall and formed a thin liquid film. As time goes by, and the liquid film thickness gradually increased with time. Han et al. [32] established the Eulerian-Lagrangian two-phase model coupled Eulerian wall film model for the gas-water separator to obtain the droplet trajectory and liquid film distribution, and validated the model experimentally. A three-field two-fluid model was developed by Li et al. [33] to simulate the post-dryout heat and mass transfer in a vertical pipe including liquid film evaporation, droplets deposition, and droplets entrainment, which was a Eulerian-Eulerian coupled Eulerian wall film model. The comparison between the simulation results of the liquid film flow rate and the experimental results of the steam-water pipe flow validated the model. Yue et al. [34] used Eulerian-Eulerian coupled Eulerian wall film model to study the influence of liquid flow rate on liquid film flow in a Gas-Liquid Cylindrical Cyclone. The results showed that high liquid flow rate impairs the uniformity of the liquid film.

As mentioned above, the existing numerical models of supersonic separators do not consider the formation of liquid film, moreover, the existing three-field two-fluid model does not consider the condensation effect, thereby it cannot be directly applied to supersonic separators. In order to study the complicated heat and mass exchange mechanism among the three fields of gas, liquid droplets and liquid film in the supersonic separator, this research proposes a novel three-field two-fluid model based on Eulerian-Eulerian approach considering homogeneous/heterogeneous condensation and interphase slip. This model has not been reported. Subsequently, the coupled heat and mass transfer was studied, and the separation performance was predicted. It provides an effective method for analyzing the three-field heat and mass transfer with the characteristics of condensation and strong swirl and optimizing the supersonic separator.

2 Three-field two-fluid model

The three-field two-fluid model based on the Eulerian-Eulerian approach for the supersonic separator includes the gas-phase governing equations, the homogeneous/heterogeneous condensation model, the Eulerian wall film model, and the heat and mass coupling between the three fields of gas, liquid droplets, and liquid film. The schematic diagram of three-field two-fluid in the supersonic separator is shown in Fig. 2 (a). The three-field two-fluid is established based on the following assumptions: (i) The liquid droplets are spherical; (ii) The latent heat released by condensation is completely absorbed in the gas phase; (iii) The homogeneous/heterogeneous condensation and interphase slip are considered; (iv) Due to the strong swirling flow, the influence of the drag force on the two-phase momentum equations is considered. (v) Due to the strong swirling flow, only the droplet deposition is considered, while the droplet entrainment is ignored.

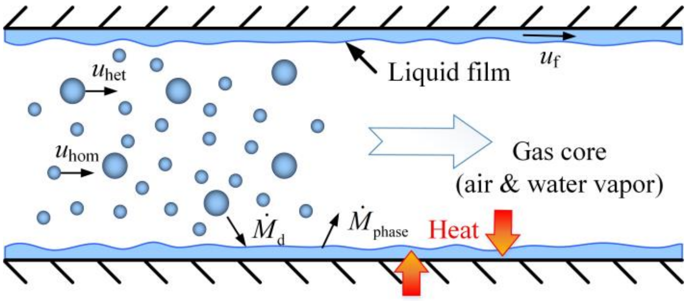

(a) Three-field two-fluid in supersonic separator

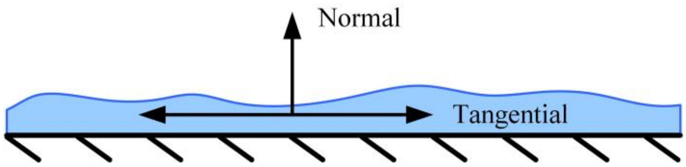

(b) Tangential and normal direction of thin liquid film

Fig. 2 Schematic diagram of modeling in supersonic separator.

2.1 Governing equations

2.1.1 Gas phase model

The mass, momentum, and energy conservation equation of gas phase (air and water vapor mixture) is governed by

$$\frac{\partial}{\partial t}\left(\alpha_{\rm g}\rho_{\rm g}\right)+\nabla\cdot\left(\alpha_{\rm g}\rho_{\rm g}\vec{u}_{\rm g}\right)=-\left(\dot{m}_{\rm hom}+\dot{m}_{\rm het}\right) \tag{1}$$

$$\frac{\partial}{\partial t}\left(\alpha_{\rm g}\rho_{\rm g}\vec{u}_{\rm g}\right)+\nabla\cdot\left(\alpha_{\rm g}\rho_{\rm g}\vec{u}_{\rm g}\vec{u}_{\rm g}\right)=-\alpha_{\rm g}\nabla p+\nabla\cdot\left(\alpha_{\rm g}\bar{\bar{\tau}}_{\rm eff}\right)+\alpha_{\rm g}\rho_{\rm g}\vec{g}-\left(\dot{m}_{\rm hom}+\dot{m}_{\rm het}\right)\vec{u}_{\rm g}-\vec{F}_{D} \tag{2}$$

$$\frac{\partial}{\partial t}\left(\alpha_{\rm g}\rho_{\rm g}E\right)+\nabla\cdot\left[\alpha_{\rm g}\left(\rho_{\rm g}E+p\right)\vec{u}_{\rm g}\right]=\nabla\cdot\left[\alpha_{\rm g}\lambda_{\rm eff}\nabla T_{\rm g}-\alpha_{\rm g}\sum_{\rm i}h_{\rm i}\vec{J}_{\rm i}+\alpha_{\rm g}\left(\bar{\bar{\tau}}_{\rm eff}\cdot\vec{u}_{\rm g}\right)\right]+\left(\dot{m}_{\rm hom}+\dot{m}_{\rm het}\right)h_{\rm lg} \tag{3}$$

where the subscript ‘g’, ‘hom’, ‘het’, and ‘i’ represent gas phase, homogenous nucleus, heterogenous nucleus, and species, respectively. $\alpha_{\rm g}$ is the volume fraction of gas phase, $\alpha_{\rm g}=1-\alpha_{\rm hom}-\alpha_{\rm het}$. $\vec{u}$ and $\vec{g}$ is the velocity and gravity vector. $\vec{J}_{\rm i}$ is the diffusion flux of species i. The ρ, p, T, E, $h_{\rm i}$, and $h_{\rm lg}$ denote the density, pressure, temperature, total energy, enthalpy of species i, and latent heat, respectively. The drag force is $\vec{F}_{\mathrm{D}} = \vec{F}_{\mathrm{D,hom}} + \vec{F}_{\mathrm{D,het}}$. The $\dot{m}_{\mathrm{hom}}$ and $\dot{m}_{\mathrm{het}}$ (kg m^{-3} s^{-1}) is droplet mass changing rate for homogenous and heterogenous condensation, respectively. λ_{eff} is the effective thermal conductivity, $\lambda_{\mathrm{eff}} = \lambda + \lambda_{\mathrm{tu}}$, where λ_{tu} represents turbulent thermal conductivity. The effective stress tensor is described by

$$\bar{\bar{\tau}}_{\mathrm{eff}} = \mu_{\mathrm{eff}} \left[\left(\nabla \vec{u}_{\mathrm{g}} + \nabla \vec{u}_{\mathrm{g}}^{\,T} \right) - \frac{2}{3} \nabla \cdot \vec{u}_{\mathrm{g}} I \right] \tag{4}$$

where I is the unit tensor, μ_{eff} is the effective molecular viscosity, $\mu_{\mathrm{eff}} = \mu + \mu_{\mathrm{tu}}$. The turbulent viscosity μ_{tu} and turbulent thermal conductivity λ_{tu} is calculated by the turbulence model. In this research, the Reynolds stress model is applied to calculate the turbulence flow.

The species transport equation of gas phase is

$$\frac{\partial}{\partial t}\left(\alpha_{\mathrm{g}} \rho_{\mathrm{g}} Y_{\mathrm{i}}\right) + \nabla \cdot \left(\alpha_{\mathrm{g}} \rho_{\mathrm{g}} \vec{u}_{\mathrm{g}} Y_{\mathrm{i}}\right) = -\nabla \cdot \left(\alpha_{\mathrm{g}} \vec{J}_{\mathrm{i}}\right) + S_{\mathrm{i}} \tag{5}$$

where Y_{i} represents the mass fraction of species i. S_{i} is source term where the value is $-(\dot{m}_{\mathrm{hom}} + \dot{m}_{\mathrm{het}})$ for the species of water vapor.

2.1.2 Dispersed droplet model

The volumetric concentration of dispersed homogeneous and heterogeneous droplet number, n_{hom} and n_{het} (m^{-3}) are expressed by

$$\frac{\partial n_{\mathrm{hom}}}{\partial t} + \nabla \cdot \left(n_{\mathrm{hom}} \vec{u}_{\mathrm{hom}}\right) = J - N_{\mathrm{c}} \tag{6}$$

$$\frac{\partial n_{\mathrm{het}}}{\partial t} + \nabla \cdot \left(n_{\mathrm{het}} \vec{u}_{\mathrm{het}}\right) = 0 \tag{7}$$

where J (m^{-3} s^{-1}) is homogeneous nucleation rate. N_{c} is the source term due to collision.

The volume fractions of homogeneous and heterogeneous droplets, α_{hom} and α_{het} are expressed as

$$\frac{\partial}{\partial t}\left(\alpha_{\mathrm{hom}} \rho_l\right) + \nabla \cdot \left(\alpha_{\mathrm{hom}} \rho_l \vec{u}_{\mathrm{hom}}\right) = \dot{m}_{\mathrm{hom}} - \dot{m}_{\mathrm{c}} \tag{8}$$

$$\frac{\partial}{\partial t}\left(\alpha_{\mathrm{het}} \rho_l\right) + \nabla \cdot \left(\alpha_{\mathrm{het}} \rho_l \vec{u}_{\mathrm{het}}\right) = \dot{m}_{\mathrm{het}} + \dot{m}_{\mathrm{c}} \tag{9}$$

where ρ_l is the droplet density. $\dot{m}_{\mathrm{c}}$ is the mass source term due to collision and coalescence. The effective density of homogenous and heterogeneous droplets is $\rho_{\mathrm{hom}} = \alpha_{\mathrm{hom}} \rho_l$ and $\rho_{\mathrm{het}} = \alpha_{\mathrm{het}} \rho_l$.

The momentum conservation equations of homogenous and heterogeneous droplets are expressed by

$$\frac{\partial}{\partial t}\left(\alpha_{\mathrm{hom}} \rho_l \vec{u}_{\mathrm{hom}}\right) + \nabla \cdot \left(\alpha_{\mathrm{hom}} \rho_l \vec{u}_{\mathrm{hom}} \vec{u}_{\mathrm{hom}}\right) = -\alpha_{\mathrm{hom}} \nabla p + \alpha_{\mathrm{hom}} \rho_l \vec{g} + \left(\dot{m}_{\mathrm{hom}} - \dot{m}_{\mathrm{c}}\right) \vec{u}_{\mathrm{hom}} + \vec{F}_{\mathrm{D,hom}} \tag{10}$$

$$\frac{\partial}{\partial t}\left(\alpha_{\mathrm{het}} \rho_l \vec{u}_{\mathrm{het}}\right) + \nabla \cdot \left(\alpha_{\mathrm{het}} \rho_l \vec{u}_{\mathrm{het}} \vec{u}_{\mathrm{het}}\right) = -\alpha_{\mathrm{het}} \nabla p + \alpha_{\mathrm{het}} \rho_l \vec{g} + \left(\dot{m}_{\mathrm{het}} + \dot{m}_{\mathrm{c}}\right) \vec{u}_{\mathrm{het}} + \vec{F}_{\mathrm{D,het}} \tag{11}$$

where $\vec{F}_{\mathrm{D,hom}}$ and $\vec{F}_{\mathrm{D,het}}$ are drag force between gas and water droplet.

2.1.3 Eulerian wall film model

The mass, momentum, and energy conservation equation of the two-dimensional film in three-dimensional domain are as follows

$$\frac{\partial}{\partial t}(\rho_l\delta)+\nabla_{\mathrm{s}}\cdot\left(\rho_l\delta\vec{u}_f\right)=\dot{m}_{\mathrm{d}}-\dot{m}_{\mathrm{phase}} \tag{12}$$

$$\frac{\partial}{\partial t}\left(\rho_l\delta\vec{u}_f\right)+\nabla_{\mathrm{s}}\cdot\left(\rho_l\delta\vec{u}_f\vec{u}_f\right)=-\delta\nabla_{\mathrm{s}}p+\rho_l\delta\vec{g}_\tau+\frac{3}{2}\vec{\tau}_{fs}-\frac{3\mu_l}{\delta}\vec{u}_f+\vec{U}_d+\left(\dot{m}_{\mathrm{d}}-\dot{m}_{\mathrm{phase}}\right)\vec{u}_f \tag{13}$$

$$\frac{\partial}{\partial t}\left(\rho_l\delta h_f\right)+\nabla_{\mathrm{s}}\cdot\left(\rho_l\delta h_f\vec{u}_f\right)=\frac{\lambda_l}{\delta}\left(T_{\mathrm{s}}+T_{\mathrm{w}}-2T_{\mathrm{m}}\right)+\left(\dot{m}_{\mathrm{d}}-\dot{m}_{\mathrm{phase}}\right)h_{\mathrm{lg}} \tag{14}$$

where ∇_{s} is the surface gradient. δ is the film thickness. $\vec{u}_f$ is film velocity vector. $\dot{m}_{\mathrm{d}}$ and $\dot{m}_{\mathrm{phase}}$ represent deposition rate, film phase change rate (kg m^{-2} s^{-1}), respectively. $\vec{g}_\tau$ is the gravity component parallel to the film. The third and fourth terms on the right-hand side of Eq.(13) represent viscous shear stress on gas-film and film-wall interfaces. $\vec{U}_d$ is the momentum source term of film. T_{s}, T_{w}, and T_{m} are the film surface, wall, and film half depth temperature, respectively.

2.2 Interphase exchange between gas and droplet

The droplet mass changing rate (condensation and evaporation rate) between the gas phase and dispersed droplets are calculated by

$$\dot{m}_{\mathrm{hom}}=J\rho_l\frac{4\pi r_{\mathrm{c}}^3}{3}+n_{\mathrm{hom}}\rho_l4\pi r_{\mathrm{hom}}^2\frac{dr_{\mathrm{hom}}}{dt},\quad \dot{m}_{\mathrm{het}}=n_{\mathrm{het}}\rho_l4\pi r_{\mathrm{het}}^2\frac{dr_{\mathrm{het}}}{dt} \tag{15}$$

The homogeneous nucleation rate J (m^{-3} s^{-1}) is calculated by [35]

$$J=\frac{\upsilon\rho_{\mathrm{g}}^2}{S_{\mathrm{s}}}\sqrt{\frac{2\sigma}{\pi m_m^5}}\exp\left(-\frac{16\pi}{3}\frac{\upsilon^2\sigma^3}{\left(k_{\mathrm{B}}T_{\mathrm{g}}\right)^3\left(\ln S_{\mathrm{s}}\right)^2}\right) \tag{16}$$

where, υ and m_{m} represent volume and mass of single water molecule. k_{B} represents Boltzmann's constant, σ (N m^{-1}) is liquid surface tension. S_{s} is the supersaturation of water vapor, $S_{\mathrm{s}}=p_{\mathrm{v}}/p_{\mathrm{s}}(T_{\mathrm{g}})$, where $p_{\mathrm{s}}(T_{\mathrm{v}})$ is the saturation pressure of water vapor at T_{v}. The critical droplet size of homogenous nucleation is calculated by

$$r_{\mathrm{c}}=\frac{2\sigma}{\rho_l R_{\mathrm{v}}T_{\mathrm{g}}\ln\left(S_{\mathrm{s}}\right)} \tag{17}$$

where R_{v} represent specific gas constant. The mean radii r_{hom} and r_{het} are expressed as

$$r_{\mathrm{hom}}=\left(\frac{3\alpha_{\mathrm{hom}}}{4\pi n_{\mathrm{hom}}}\right)^{\frac{1}{3}},\qquad r_{\mathrm{het}}=\left(\frac{3\alpha_{\mathrm{het}}}{4\pi n_{\mathrm{het}}}\right)^{\frac{1}{3}} \tag{18}$$

The growth rate of droplet in condensation and evaporation processes is calculated by

$$\frac{dr}{dt} = \frac{1}{\rho_l h_{\mathrm{lg}}}\left(T_{\mathrm{r}} - T_{\mathrm{v}}\right)\sum_{\mathrm{i}=1}^{2} a_{\mathrm{i}} \tag{19}$$

where the subscript 'v' represents water vapor. a_{i} is the heat transfer coefficient between the water droplet and species i [8]. The droplet surface temperature T_{r} is calculated by

$$T_{\mathrm{r}} = T_{\mathrm{d}}\left(p_{\mathrm{v}}\right) - D_{\mathrm{T}}\frac{r_{\mathrm{c}}}{r} \tag{20}$$

where D_{T} is subcooling, $D_{\mathrm{T}} = T_{\mathrm{d}}(p_{\mathrm{v}}) - T_{\mathrm{g}}$. $T_{\mathrm{d}}(p_{\mathrm{v}})$ is the dew point temperature at p_{v}.

Generally, the size and slip velocity of heterogeneous droplets (foreign droplet) are significantly greater than those of homogeneous droplets, since the diameter of homogeneous droplets is generally below 0.1 μm [30][36]. Thus, the heterogeneous droplets as collectors collide with the surrounding smaller size homogeneous droplets. The mean collision frequency f is expressed as [37]

$$f = n_{\mathrm{hom}}\pi\left(r_{\mathrm{het}} + r_{\mathrm{hom}}\right)^2\left|\vec{u}_{\mathrm{het}} - \vec{u}_{\mathrm{g}}\right| \tag{21}$$

Therefore, the source term of Eq.(6) is

$$N_{\mathrm{c}} = n_{\mathrm{het}} f \tag{22}$$

The homogeneous droplets are collected by heterogeneous droplets, whose mass is transferred to the heterogeneous droplets, thereby the heterogeneous droplet radius increases up gradually. The mass source term due to coalescence is calculated by

$$\dot{m}_{\mathrm{c}} = n_{\mathrm{het}} f \rho_l \frac{4\pi r_{\mathrm{hom}}^3}{3} \tag{23}$$

The drag force between the continuous and dispersed droplets in Eq.(2) is defined as [38]

$$\vec{F}_{\mathrm{D,hom}} = \frac{9\mu_{\mathrm{g}}}{2r_{\mathrm{hom}}^2}C_{\mathrm{D}}\frac{\mathrm{Re}_{\mathrm{p,\,hom}}}{24}\alpha_{\mathrm{hom}}\left(\vec{u}_{\mathrm{g}} - \vec{u}_{\mathrm{hom}}\right),\quad \vec{F}_{\mathrm{D,het}} = \frac{9\mu_{\mathrm{g}}}{2r_{\mathrm{het}}^2}C_{\mathrm{D}}\frac{\mathrm{Re}_{\mathrm{p,\,het}}}{24}\alpha_{\mathrm{het}}\left(\vec{u}_{\mathrm{g}} - \vec{u}_{\mathrm{het}}\right) \tag{24}$$

where the relative Reynolds number $\mathrm{Re}_{\mathrm{p,hom}}$ and $\mathrm{Re}_{\mathrm{p,het}}$ are expressed as

$$\mathrm{Re}_{\mathrm{p,hom}} = 2\rho_{\mathrm{g}} r_{\mathrm{hom}}\left|\vec{u}_{\mathrm{hom}} - \vec{u}_{\mathrm{g}}\right| / \mu_{\mathrm{g}},\quad \mathrm{Re}_{\mathrm{p,het}} = 2\rho_{\mathrm{g}} r_{\mathrm{het}}\left|\vec{u}_{\mathrm{het}} - \vec{u}_{\mathrm{g}}\right| / \mu_{\mathrm{g}} \tag{25}$$

The drag coefficient C_{D} is expressed as [39]

$$C_{\mathrm{D}} = \begin{cases} \frac{24}{\mathrm{Re_p}}, & \mathrm{Re_p} \le 1 \\ \frac{24}{\mathrm{Re_p}}\left(1 + 0.15\mathrm{Re_p^{0.687}}\right), & 1 < \mathrm{Re_p} \le 1000 \\ 0.44, & \mathrm{Re_p} > 1000 \end{cases} \tag{26}$$

For smaller Reynolds numbers, the molecular viscous force dominates. However, when the particle size is small enough to approach the gas molecules free path length (Knudsen number Kn > 1), the drag coefficient should be corrected by Cunningham slip correction factor, $C_{\mathrm{D}} = \frac{24}{\mathrm{Re_p} C_{\mathrm{C}}}$, where Cunningham slip correction factor is calculated by [40]

$$C_c = 1 + 2\mathrm{Kn}_g \left(1.257 + 0.4 e^{-1.1/(2\mathrm{Kn}_g)}\right) \quad (27)$$

2.3 Coupling of the gas core with liquid film

The deposited droplets to the wall will gradually form a liquid film, that is, their mass and momentum will be removed from the dispersed phase and added to the liquid film equations as source terms. The droplet deposition rate, that is, the mass source term of liquid film $\dot{m}_d$ (kg m^{-2} s^{-1}) is given by [41]

$$\dot{m}_d = \dot{m}_{d,hom} + \dot{m}_{d,het} = \alpha_{hom}\rho_l \vec{u}_{hom} \cdot \vec{n} + \alpha_{het}\rho_l \vec{u}_{het} \cdot \vec{n} \quad (28)$$

where $\vec{n}$ is film area normal.

The momentum source term of liquid film is

$$\vec{U}_d = \vec{U}_{d,hom} + \vec{U}_{d,het} = \dot{m}_{d,hom}\vec{u}_{t,hom} + \dot{m}_{d,het}\vec{u}_{t,het} \quad (29)$$

where film tangential velocity vector is $\vec{u}_t = \vec{u} - (\vec{u} \cdot \vec{n})\vec{n}$. The tangential and normal directions of thin liquid film are shown in Fig. 2 (b).

The phase change rate between wall film and gas phase (kg m^{-2} s^{-1}) is calculated by [42]

$$\dot{m}_{phase} = \frac{\rho_g M/d}{\rho_g M/d + C_{phase}} C_{phase}\left(Y_s - Y\right) \quad (30)$$

where d represents cell-center-to-wall distance. M is the mass diffusivity of water vapor. C_{phase} is the phase change constant. Y_s represent saturation mass fraction of water vapor. Y is the mass fraction of water vapor at the cell-center of near-wall cell.

3 CFD validation

3.1 Numerical scheme

ANSYS FLUENT software is used for numerical simulation. The conservation equations of dispersed droplets are implemented through the User-Defined-Scalar interface. The mass and thermal coupling between the discrete droplets and the gas phase and it between the liquid film and the discrete droplets are realized by establishing source terms through the User-Defined-Function interface. Because the conditions of this study are low pressure and normal temperature, it is reasonable to approximate the gas phase as an ideal gas. The separator and applies Reynolds stress model (RSM) to calculate turbulence, and other cases apply transition SST model. The density-based solver is employed to calculate the supersonic flow, and the pressure-based solver is used to calculate the low-speed flow. Coupling Eulerian wall film model must adopt a pressure-based solver. For the supersonic nozzle, the solution method adopts implicit formulation and Roe-FDS flux type. The least squares cell-based format is chosen for the gradient discretization. The second order upwind discrete scheme is applied to ensure higher calculation accuracy. For other cases, the solution method adopts SIMPLE scheme pressure-velocity coupling, and the pressure discretization adopts

PRESTO! format. In this study, the convergence criteria for all dependent variables are lower than 1.0×10^{-4}. For the supersonic separator and supersonic nozzle, the air-water vapor two-phase flow as working fluid. The inlet boundary condition is set to pressure-inlet, and the outlet boundary condition is set to pressure-outlet. The air as working fluid in the cyclone separator. The inlet boundary condition is the velocity-inlet, and the outlet boundary condition is the outflow. There is an air-water vapor two-phase flow in the rectangular channel, the inlet boundary condition is the velocity-inlet. The outlet boundary condition is the pressure-outlet.

3.2 Experimental validation

According to the characteristics of the flow and heat transfer in the supersonic separator, the experimental validation can be divided into the following three parts: validating the supersonic condensing flow in the supersonic nozzle; validating the strong swirling flow in the cyclone separator; validating the liquid film flow and liquid film phase change in the rectangular channel. Consequently, the calculation accuracy of the model for condensate flow, swirl separation, and liquid film flow is validated successively.

3.2.1 Condensation flow in supersonic nozzle

The geometry of the 3D axisymmetric supersonic nozzle is shown in Fig. 3 (a), and the nozzle throat diameter is 10 mm. The experimental platform for homogeneous condensation of the supersonic nozzle had been explained in our previous article [8]. The grid is structured hexahedral grid, which is refined on the wall to satisfy the requirement $y^+ < 1$. The grid independence tests are carried based on Grid Convergence Index (GCI) analysis [43]. The GCI is a method of mesh refinement error estimation based on generalized extrapolation theory, which is described by

$$GCI = \frac{F_s\left|\varepsilon\right|}{r^p - 1}\times 100\% \tag{31}$$

where F_s is the safety factor and its empirical value is 3, ε is the relative error between two grids, r is the refinement factor ratio, and p is the algorithm accuracy order. A small GCI means that the difference between the solution results of the two grids is small. The three groups of grids are grids 1: 16,200 cells, grids 2: 13,000 cells, and grids 3: 10,000 cells, respectively. Taking the outlet pressure as the test parameter, as shown in Table 1, 13,000 grid cells can gain grid-independent solutions.

Table 1 Test results of Grid Convergence Index.

		Grids 1-2 (1-fine, 2-medium)		Grids 2-3 (2-medium, 3-coarse)	
F_s	p	$\varepsilon_{1,2}$ (%)	$GCI_{1,2}$ (%)	$\varepsilon_{2,3}$ (%)	$GCI_{2,3}$ (%)
3	3	0.17	0.87	0.65	2.74

The inlet pressure of the supersonic nozzle is 300 kPa, the inlet temperature is 50°C, and the outlet is supersonic flow. The pressure distribution along the nozzle is shown in Fig. 3 (b). It can be seen that the simulation data of the back-pressure ratio is in good agreement with the experiment with different humidity conditions, which validates that the established CFD model can maintain a high-precision simulation of supersonic condensing flow.

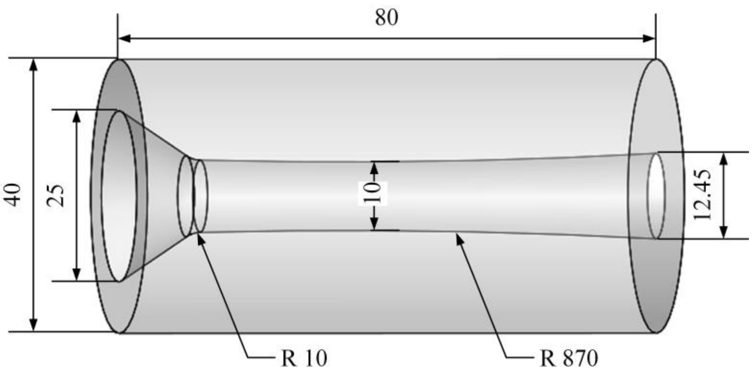

(a) Geometry of supersonic nozzle (mm)

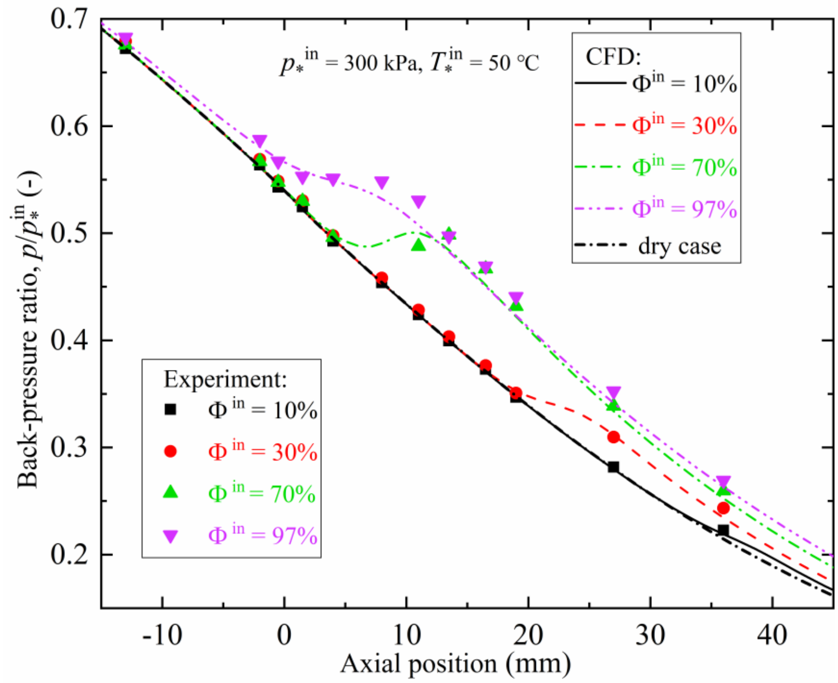

(b) Comparison of pressure between CFD and experiment

Fig. 3 Comparison between CFD and experiment of supersonic nozzle.

3.2.2 Dispersed phase behaviors in cyclone separator

The geometry and grid of the cyclone separator are shown in Fig. 4. The structured hexahedral grid is generated. When the number of grid cells is 218277, a grid-independent solution can be obtained. The released particles are typical cement raw materials. The characteristic diameter of the particles is 29.9 μm. The air and particles enter the cyclone separator at the same speed and are separated by the centrifugal force. For other boundary conditions, please refer to the articles of Wang et al. [44]

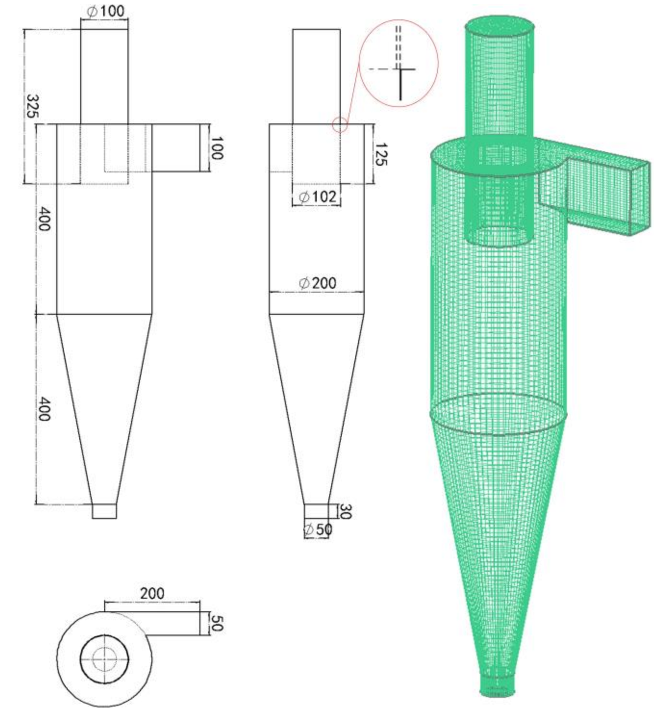

Fig. 4 Geometry and grid diagram of cyclone separator (mm).

The tangential velocity distribution in the cyclone separator is shown in Fig. 5 (a). It can be seen that the maximum error between the simulation and the experiment data of the tangential velocity is about ±5%. The comparison between the simulation and the experiment results of the collection efficiency at different inlet velocities is shown in Fig. 5 (b). It can be seen that the inlet velocity is 15-30 m s^{-1}, the simulation and experiment of the collection efficiency are in the highest agreement. The above results validate that the established model can maintain high accuracy in simulating the particle behaviors in strong swirling flow.

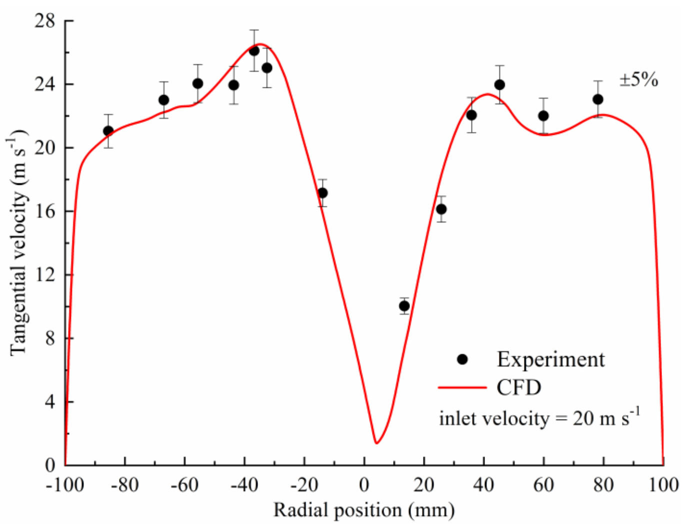

(a) Comparison of tangential velocity

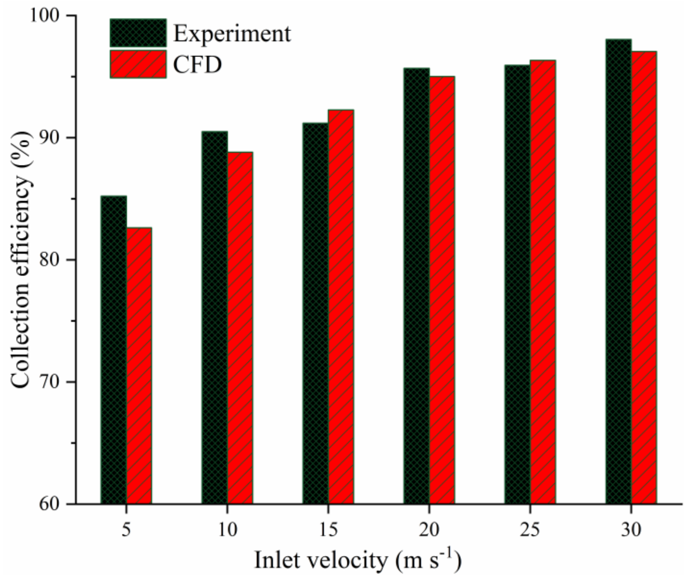

(b) Comparison of collection efficiency

Fig. 5 Comparison between CFD and experiment in cyclone separator.

3.2.3 Liquid film flow and film evaporation

The 3D computational domain and grid of the rectangular channel are shown in Fig. 6. The structural hexahedral grid is generated and refined in the near-wall area to meet the boundary layer calculation requirement $y^+ < 1$. Simultaneously, in order to calculate the liquid film flow and liquid film evaporation more accurately, the grid is further refined within the initial liquid film height of the bottom wall. After the grid independence test, the number of grid cells is determined to be 960,687. The liquid film flows downward from the top of the vertical rectangular channel into the calculation domain. The air flows upward from the bottom of the channel into the calculation domain, forming a countercurrent with the liquid film. The inlet air temperature is 45°C. and the outlet pressure is 1 atm. The initial film mass flux and incoming film temperature are setup. The heating temperature of the bottom wall is setup to evaporate the liquid film. For other boundary conditions, please refer to the articles of Du et al. [45]

The average heat flux and liquid film evaporation rate of the bottom wall are shown in Fig. 7. It can be seen that the errors of their simulation and experimental results are within ±10%. This means that the established model can simulate the liquid film flow and the heat and mass exchange between the liquid film and the moist air.

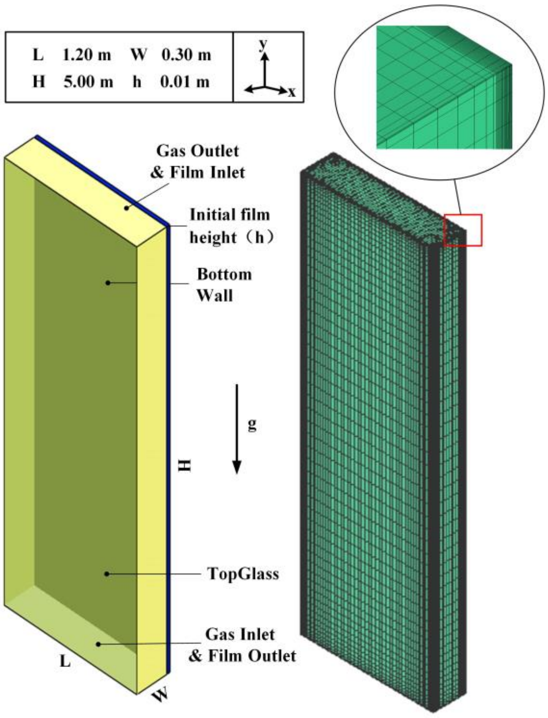

Fig. 6 3D computational domain and grid of rectangular channel.

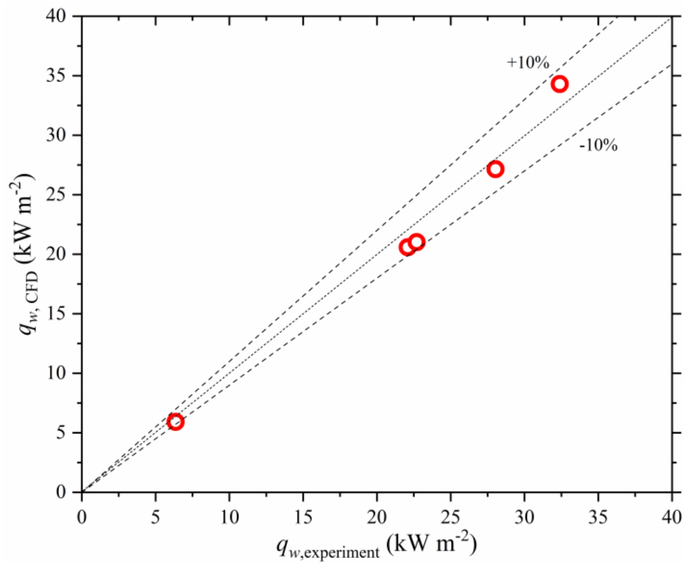

(a) Comparison of the average surface heat flux

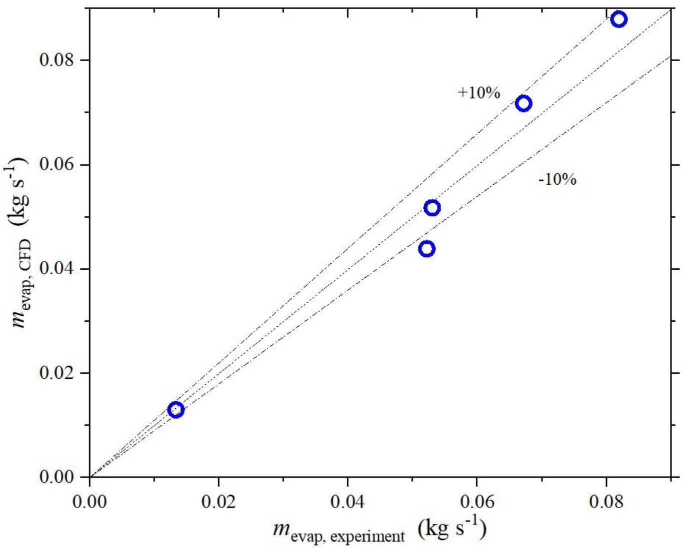

(b) Comparison of the average surface liquid film evaporation rate

Fig. 7 Comparison between CFD and experiment in the bottom wall of rectangular channel.

4 Results and discussion

The geometry and grid of the supersonic separator are shown in Fig. 8. The 3D computational domain of the supersonic separator is the annular channel between the inner center body and the outer shell, and its throat cross-sectional area is 105.07 mm^2. The type of grid is the structured hexahedron, which is refined in the near-wall area to meet the boundary layer calculation requirements. According to the grid independence test, the number of grid cells is 549,900.

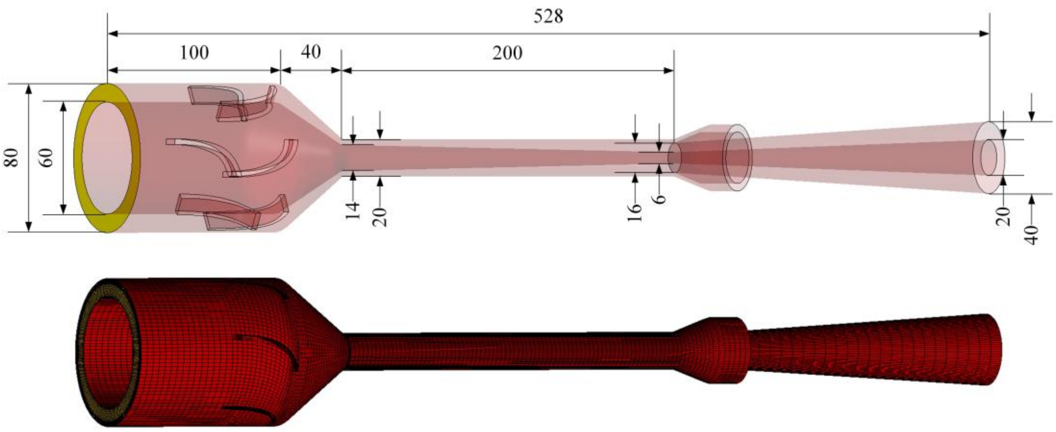

Fig. 8 Geometry and grid diagram of supersonic separator A.

4.1 *Flow field and droplet behaviors*

The common boundary conditions are p_*^{in} = 250 kPa, T_*^{in} = 30°C, Φ_*^{in} = 100% (namely p_v^{in} = 4246 Pa), p^{out} = 100 kPa. The ρ_{het}^{in} and n_{het}^{in} is specified for the boundary conditions of heterogeneous condensation, the settings of Case 1-5 are shown in Table 2. The supersonic separator B differs from supersonic separator A in that the inlet diameter is 10 mm smaller. It can be seen from Table 2 that case1-4 have the same inlet heterogeneous nucleus radius r_{het}^{in} but the different inlet heterogeneous nucleus effective density ρ_{het}^{in}. The ρ_{het}^{in} represents the number of foreign droplets injected into the inlet. According to our previous research, the optimal foreign droplet radius of separator A and separator B are about 1.0 μm and 0.3 μm [8], respectively.

Table 2 Cases of different foreign droplets in supersonic separators.

Cases	Separators	r_{het}^{in} (μm)	ρ_{het}^{in} (kg m^{-3})	n_{het}^{in} (m^{-3})	Q_{het}^{in} (ml min^{-1})
Case 1	Separator A	1.0	0.001	2.39×10^{11}	1.73
Case 2	Separator A	1.0	0.01	2.39×10^{12}	17.09
Case 3	Separator A	1.0	0.05	1.19×10^{13}	84.14
Case 4	Separator A	1.0	0.1	2.39×10^{13}	165.97
Case 5	Separator B	0.3	0.01	8.86×10^{13}	19.03

The velocity streamline of the supersonic separator A is shown in Fig. 9. After the expansion and cooling process of the supersonic nozzle, the moist gas maintains supersonic speed in the divergent section of the nozzle. The maximum gas phase velocity and subcooling degree can reach 514.4 m s^{-1} and 45.2℃, respectively. At the liquid separation position, a sudden decrease in velocity can be observed from Fig. 9 which means that a shock wave has occurred there. However, the velocity at the liquid separation position is not completely reduced to subsonic speed, so which in the diffuser further increase to supersonic speed. The shock wave phenomenon at the liquid separation position will affect the heat and mass exchange between gas and liquid, making the condensed droplets evaporate, which should be avoided as much as possible to obtain a higher separation efficiency.

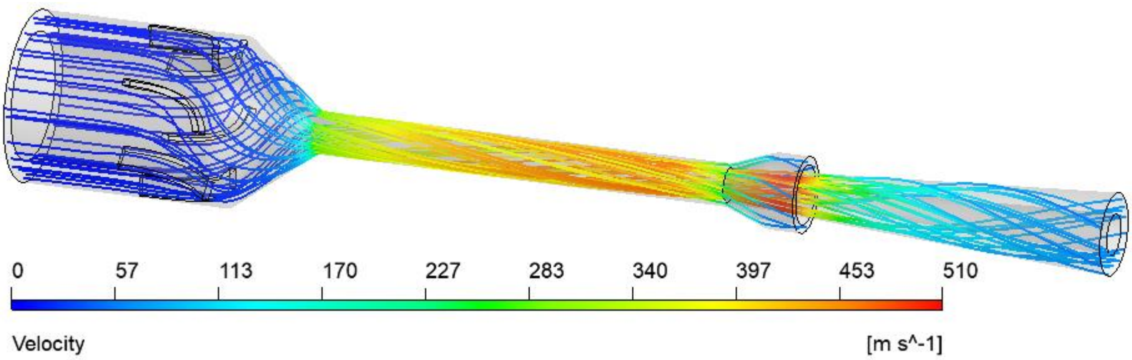

Fig. 9 Velocity streamline of the gas phase in supersonic separator A (Case2).

The tangential velocities of the supersonic separators with different inlet diameters are shown in Fig.

10, which is closely related to separation efficiency. The high tangential velocity distribution of the supersonic separator A is close to the liquid separation position, which of the supersonic separator B is close to the throat. The reduced height of the swirling blades decreases the swirl strength. The maximum swirl strength is shown in Table 3. The maximum swirl strength S_{max} of the supersonic separator B can reach 0.42, which is about twice that of the supersonic separator A.

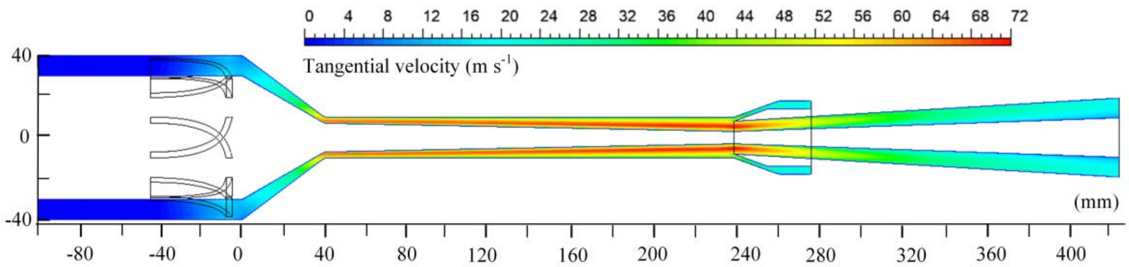

(a) Tangential velocity in supersonic separator A

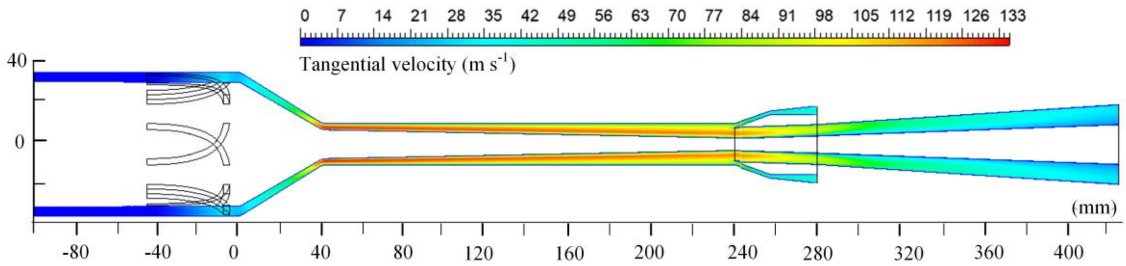

(b) Tangential velocity in supersonic separator B

Fig. 10 The contours of tangential velocity u_t on axial profile (Case2).

Table 3 Maximum tangential velocity and centrifugal acceleration of different supersonic separators.

Separators	Inlet diameter (mm)	$u_{t,max}$ (m s^{-1})	$a_{c,max}$ (m s^{-2})	S_{max} (-)
A	80	71.74	1.04×10^6	0.23
B	70	134.43	3.08×10^6	0.42

The dehydration performance of the supersonic separator can be seen from the mole fraction and partial pressure of water vapor at the dry gas outlet. As can be seen from Fig. 11 (a) and (b), after supersonic separation, the saturated water vapor is basically discharged from the wet gas outlet, which can achieve high separation efficiency. It can be clearly observed from Fig. 11 (b) that the condensation of water vapor makes a rapid decrease in the water vapor partial pressure near the nozzle throat. In the process of approaching the liquid separation position, a large number of droplets in the near-wall area evaporate under the action of the hot gas flow and shock wave, which is not conducive to water separation.

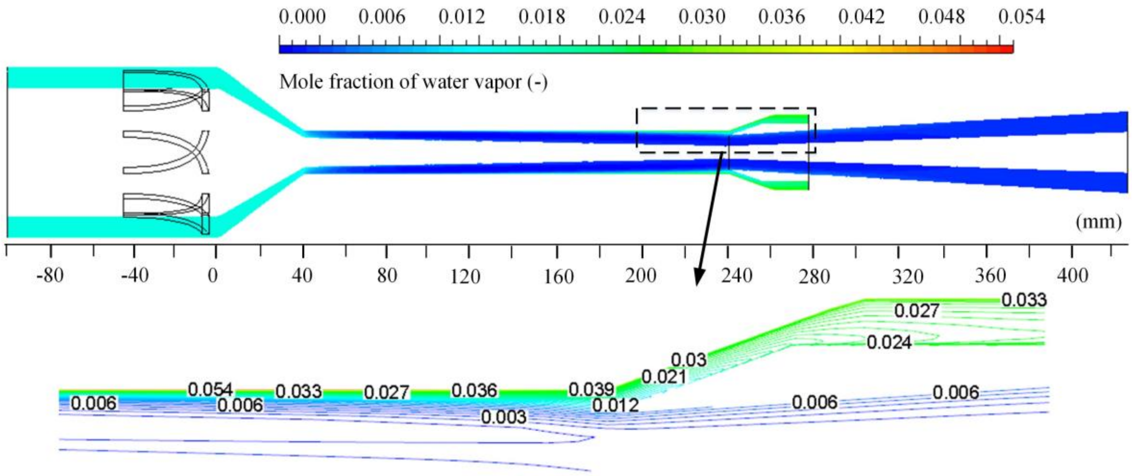

(a) The contour of mole fraction of water vapor χ_v on axial profile (Case2)

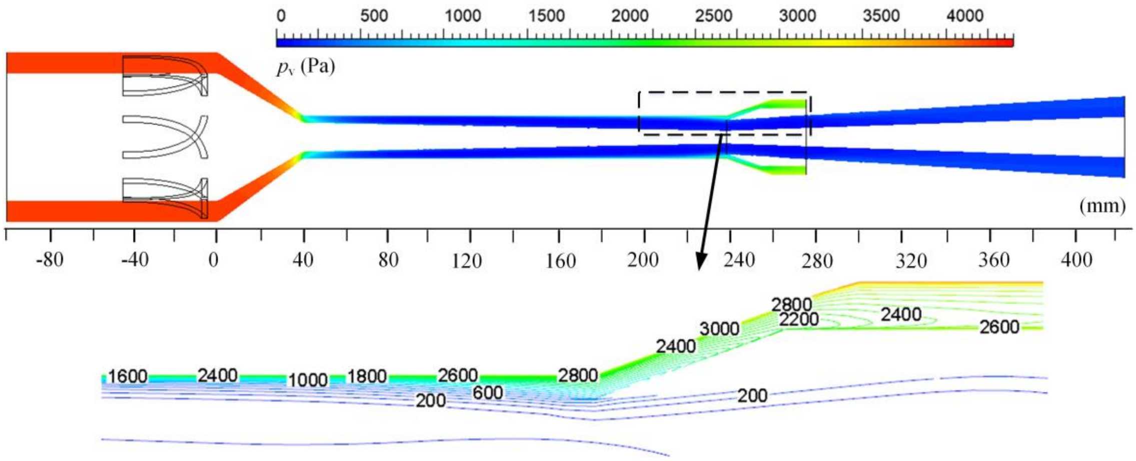

(b) The contour of water vapor partial pressure on axial profile (Case2)

Fig. 11 The distributions of mole fraction and partial pressure of water vapor.

The droplet distribution in the supersonic separator is shown in Fig. 12. It can be seen from Fig. 12 (a) that the condensation of droplets starts near the nozzle throat, and the maximum droplet mass change rate $\dot{m}_{\text{het}}$ = 412.0 kg m^{-3} s^{-1}. The droplet evaporation occurs in the near-wall area and the wet gas outlet, and the maximum droplet evaporation is -283.1 kg m^{-3} s^{-1}.

Fig. 12 (b) and Fig. 12 (c) reveal that the droplets gradually gather towards the wall and form a liquid film under the action of centrifugal force. Different from the numerical model without considering the liquid film (refer to our previous research [8]), after the dispersed droplets are centrifuged to the wall, they are not absorbed into the wall and discharged along the wall in the form of dispersed droplets. Instead, they are removed from the dispersed droplets and deposited to form a liquid film on the wall. The formed liquid film also has a heat and mass exchange process with the gas phase. The model without considering the liquid film over-predicts the separation efficiency, which will be described in the following section. Therefore, as shown in Fig. 12 (b), the droplets begin to condense and grow at the throat of the nozzle. The droplet effective density and radius gradually increase, while the droplet effective density begins to decrease after the axial position x_a = 120 mm, which means that most of the dispersed droplets are deposited to form a liquid film. The droplets coalesce under the action of centrifugal force, resulting in the further increase of droplet size, and the maximum droplet size is 1.6 μm.

Combining Fig. 12 (b) and Fig. 12 (c), it can be seen that some droplets enter the dry gas outlet. The average droplet effective density at the dry gas outlet of Case1-4 is 3.85×10^{-03} kg m^{-3}, 1.59×10^{-06} kg m^{-3}, 1.45×10^{-06} kg m^{-3}, 1.59×10^{-06} kg m^{-3}, respectively. It means that when the effective density of foreign droplets ρ_{het}^{in} = 0.001 kg m^{-3}, a large number of droplets enter the dry gas outlet, resulting in low separation efficiency. The droplet size distribution along the axial direction under different ρ_{het}^{in} is shown in Fig. 12 (d). It can be seen that when the ρ_{het}^{in} is small, the droplet size is larger. The maximum droplet size of Case1-4 is 2.50 μm, 1.59 μm, 1.51 μm, 1.48 μm, respectively.

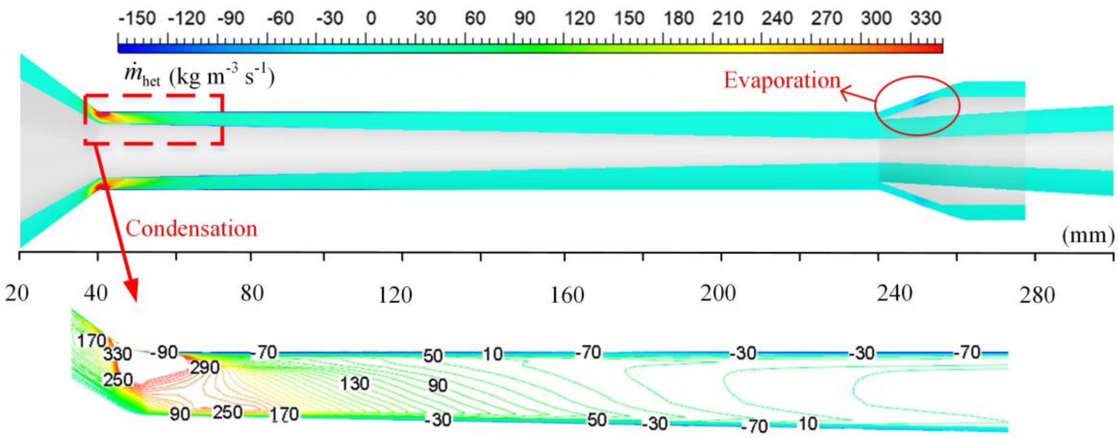

(a) The contour of droplet mass changing rate $\dot{m}_{het}$ on axial profile (Case2)

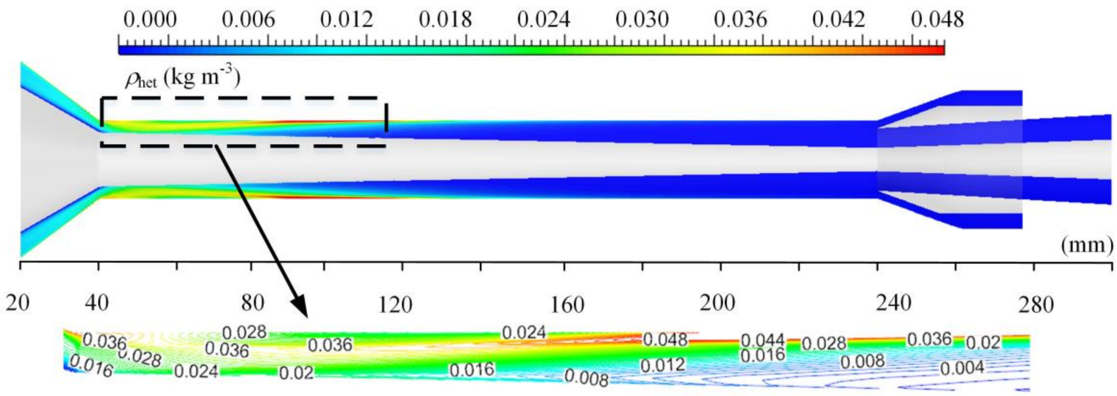

(b) The contour of effective density ρ_{het} on axial profile (Case2)

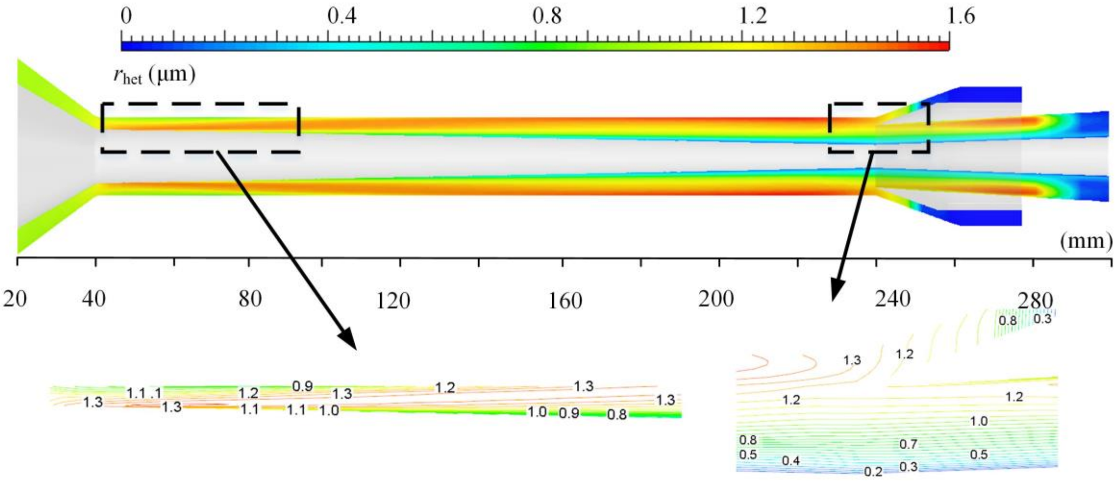

(c) The contour of droplet radius r_{het} on axial profile (Case2)

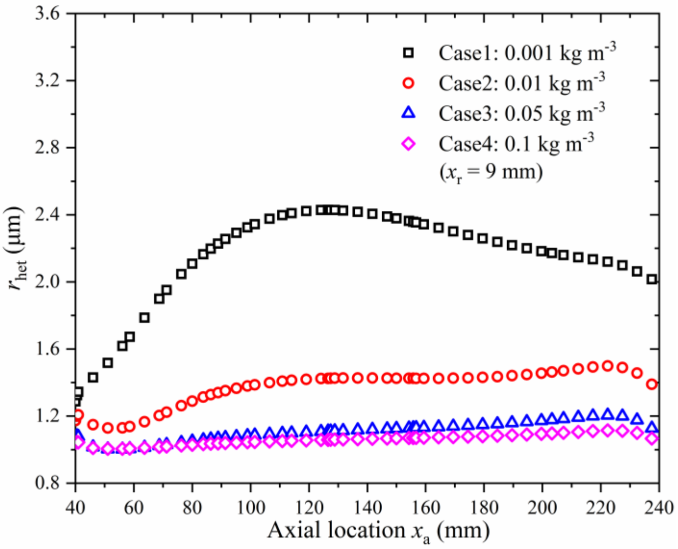

(d) Axial distributions of droplet radius r_{het} at x_r = 9 mm with different ρ_{het}^{in}

Fig. 12 The parameter distribution of droplet phase inside supersonic separator.

The droplet surface temperature, the gas phase temperature, and the latent heat are shown in Fig. 13, which reflects the heat transfer between the dispersed droplets and the gas phase. The gas phase expands in the divergent section of the nozzle, and the gas phase temperature gradually decreases, causing the wet steam to condense to form dispersed droplets. The latent heat released by the condensation is transferred to the gas phase, causing the temperature of the gas phase to slightly increase. Compared with the droplet surface temperature, the gas phase temperature is lower in the low temperature zone and higher in the high temperature zone. The heat transfer occurs from dispersed droplets to the gas phase during the condensation process (the maximum latent heat is 5.3×10^8 J m^{-3}), which occurs from the gas phase to dispersed droplets during the evaporation process (the minimum latent heat is -3.4×10^8 J m^{-3}).

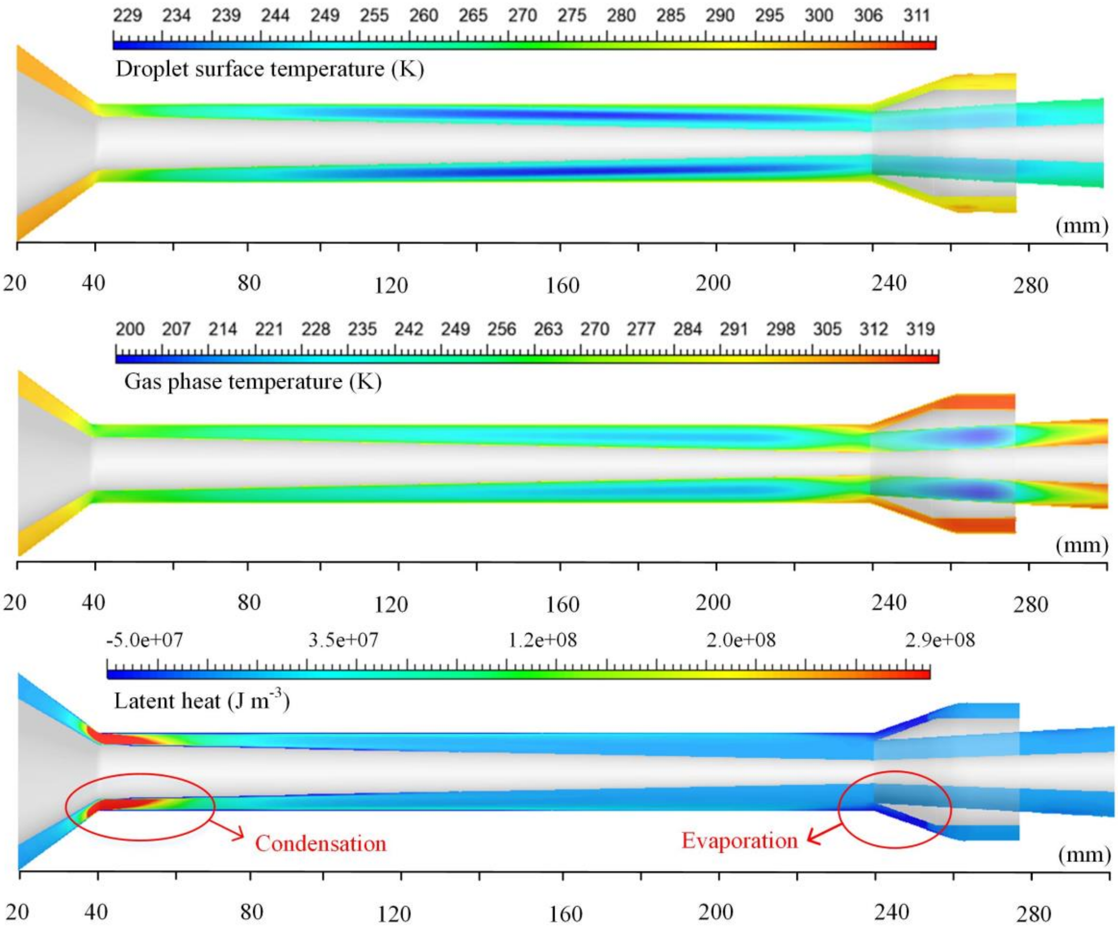

Fig. 13 The heat transfer of supersonic separator A.

The interphase slip velocity characterizes the momentum coupling between the droplet and the gas phase. The slip velocity is defined as the droplet velocity minus the gas velocity. The distribution of axial and centrifugal (radial) slip velocity components is shown in Fig. 14. It can be seen that the slip velocity before the liquid separation position gradually increases along the flow direction, which means that the drag force between the gas phase and the dispersed droplets gradually increases. The slip velocity of ρ_{het}^{in} = 0.01 kg m^{-3} is greater than that of ρ_{het}^{in} = 0.1 kg m^{-3}. Combined with Fig. 12 (d), this is because the larger the droplet size (ρ_{het}^{in} = 0.01 kg m^{-3}), the stronger the droplet inertia. Under the action of centrifugal force, the centrifugal slip velocity increases gradually, and the centrifugal velocity of droplet is greater than that of gas phase by a maximum of 24.9 m s^{-1}, so as to realize gas-liquid separation.

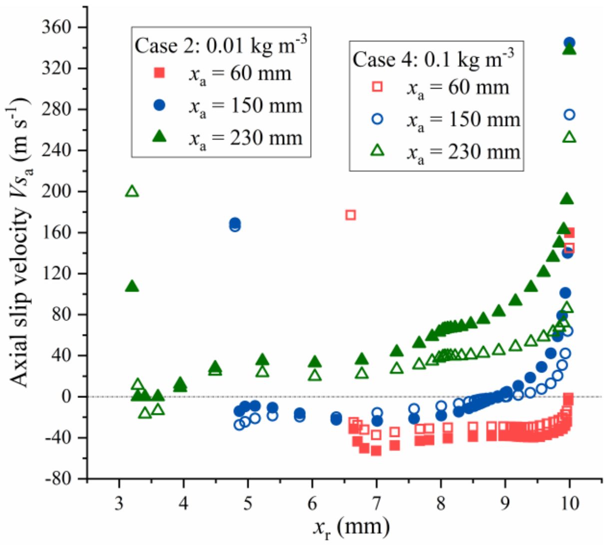

(a) Axial slip velocity for Case 2 and Case 4

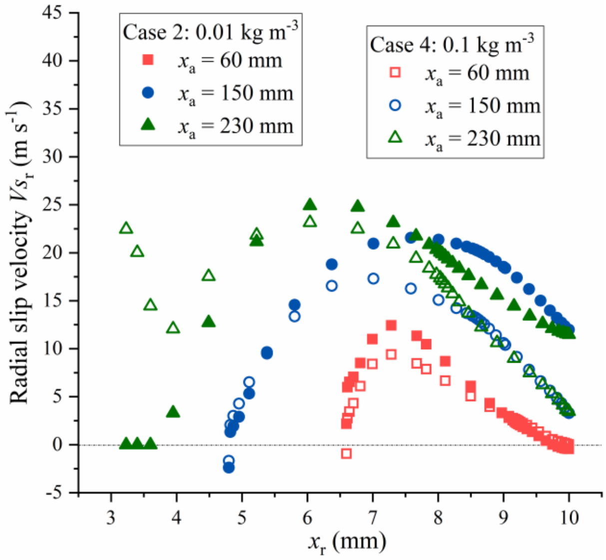

(b) Centrifugal slip velocity for Case 2 and Case 4

Fig. 14 Distribution of axial and centrifugal slip velocity components with different ρ_{het}^{in}.

4.2 Liquid film behaviors

The liquid film distribution of supersonic separator A is shown in Fig. 15. It can be seen from Fig. 15 (a) that the condensed droplets are centrifuged to the wall surface and form a liquid film, and then discharged from the wet gas outlet. The liquid film is thicker at the corner of the wet gas outlet, as shown in Fig. 15 (c), this is because the circular liquid film flow is formed there. The film thickness of swirling liquid film flow of Case1-4 at wet gas outlet is 21 μm, 47 μm, 74 μm, and 89 μm, respectively. With the increase of ρ_{het}^{in}, the thickness of liquid film increases. The maximum liquid film velocity is 1.9 m s^{-1} at x_a = 130 mm. The film phase change rate $\dot{M}_{phase}$ represents the mass exchange between the liquid film and the gas phase. A negative film phase change rate represents condensation, and a positive film phase change rate represents evaporation. As shown in Fig. 15 (a), at x_a = 120-220 mm, vapor phase condensation increases the liquid film mass.

The film temperature and heat flux reflect the heat transfer of the liquid film. As shown in Fig. 15 (b), the heat transfer of the liquid film includes the coupled heat transfer between the dispersed droplets and the gas phase, as well as the wall heat conduction. The dispersed droplets gradually form a liquid film near the axial position x_a = 120 mm, where the liquid film temperature decreases to a minimum 304.1 K due to the deposition of the dispersed droplets, where the maximum heat flux is 0.74 MW m^{-2}. Afterwards, the wall transfers heat to the cold liquid film, causing the liquid film temperature to rise. Behind the shock wave, the liquid film evaporates and reduces the liquid film temperature.

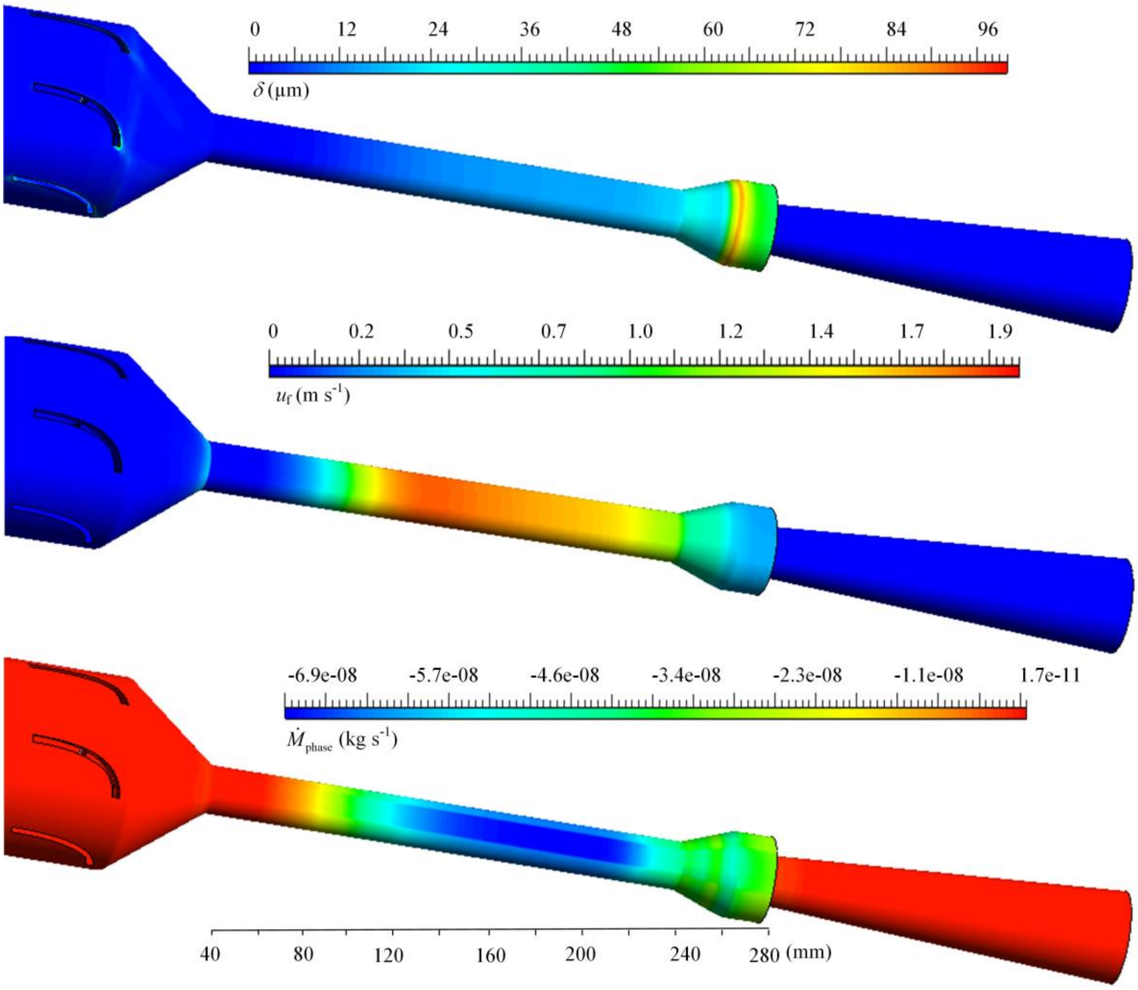

(a) Distribution of liquid film parameters (Case 2)

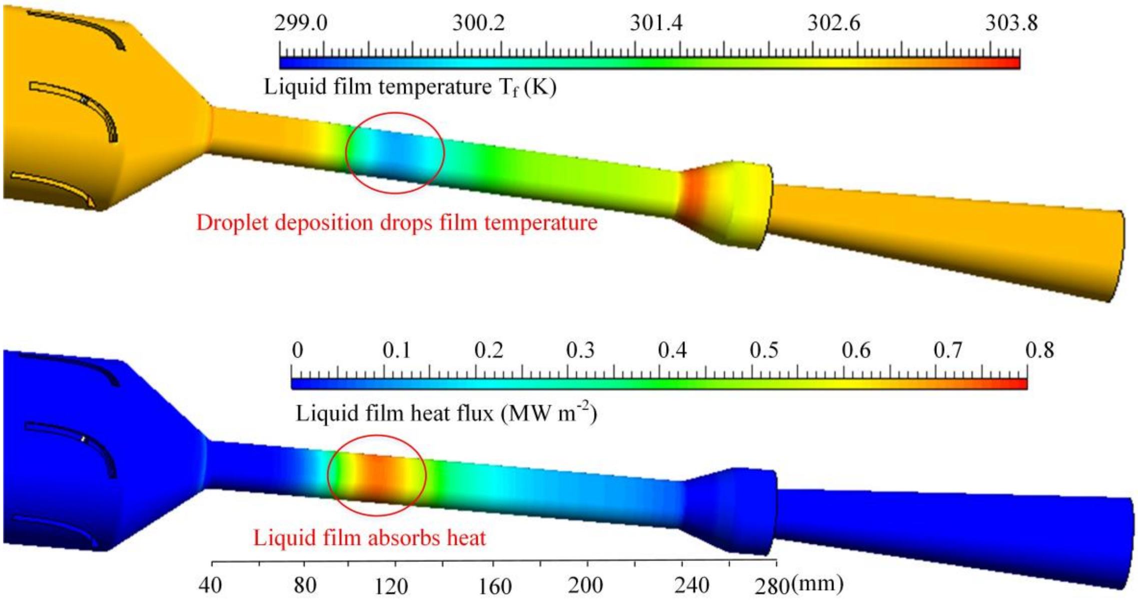

(b) Liquid film heat transfer (Case 2)

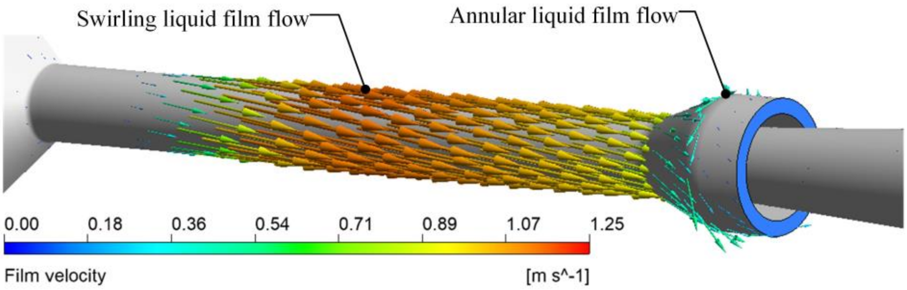

(c) Liquid film velocity streamline diagram (Case 1)

Fig. 15 Liquid film distribution of supersonic separator A.

The interfacial wave velocity plays a crucial role in the process of liquid film mass transfer. In this research, the cross-correlation principle is used to obtain the frequency and velocity of interfacial wave. The cross-correlation algorithm is implemented. The cross-correlation principle is based on the analysis of the similarity between the upstream and downstream of the signal, thereby the wave velocity measurement can be converted into a time interval measurement. Firstly, it is necessary to collect the time-dependent liquid film thickness δ_1 and δ_2 at two positions x_1 and x_2, which separated by a certain distance x_l, and the sampling frequency is set to 40 kHz. Then, the fluctuation of the liquid film thickness y_1 and y_2 are calculated, and the time-frequency domain conversion is performed. The cross-correlation function $R_{12}(\tau)$ is used to calculate the correlation between the two signals y_1 and y_2. The cross-correlation function $R_{12}(\tau)$ is expressed as [46]

$$R_{12}(\tau)=\lim_{T\to\infty}\frac{1}{T}\int_0^T y_1(\tau)y_2(t-\tau)dt \tag{32}$$

where y_1 represents the fluctuation of film thickness at position x_1, and y_2 represents the fluctuation of film thickness at position x_2.

The interfacial wave velocity u_w is calculated by

$$u_w = \frac{x_l}{\tau_0} \tag{33}$$

where the time τ_0 corresponding to the peak of $R_{12}(\tau)$ is the transit time of the signal, $x_l = x_2 - x_1$ is transit distance.

The interfacial wave velocity calculation process of Case 4 is shown in Fig. 16. The time-dependent liquid film thickness data at wet gas outlet x_1 = 270 mm and x_2 = 275 mm (x_l = 5mm) are collected in Fig. 16 (a). The fluctuation of interfacial wave can be seen from Fig. 16 (b), and y_1 is obviously lagging behind y_2. The dominant frequency f_w = 11.07 Hz (Case 4) of the interfacial wave is obtained through time-frequency domain transformation. As shown in Fig. 16 (c), the transit time τ_0 = 3.35 ms is calculated by the cross-correlation function. The maximum cross-correlation coefficient can reach 0.93. Thus, the interfacial wave velocity can be calculated as 1.49 m s^{-1}.

Table 4 shows the dominant frequency and interfacial wave velocity with different ρ_{het}^{in}. With the increase of the ρ_{het}^{in}, the thickness of the liquid film will increase. The large ρ_{het}^{in} increases the frequency and velocity of the interfacial wave, which increases the instability in the supersonic separator. The correlation coefficient decreases with the increase of the ρ_{het}^{in}, so as to the complexity of interfacial waves increases.

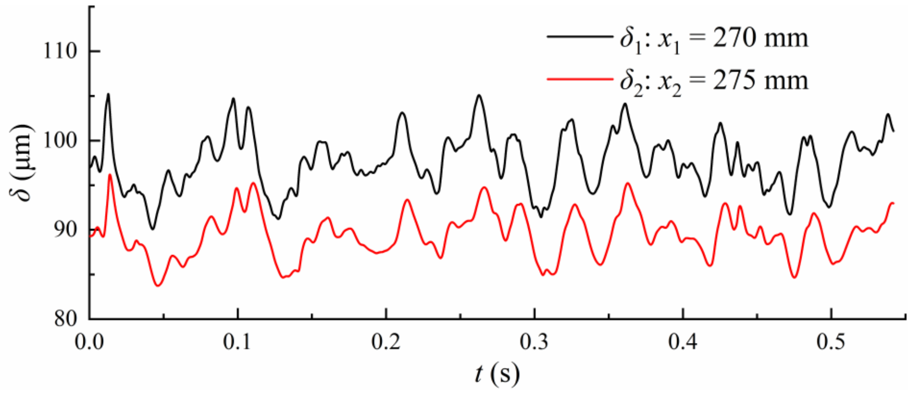

(a) Raw data of liquid film thickness obtained by data collection

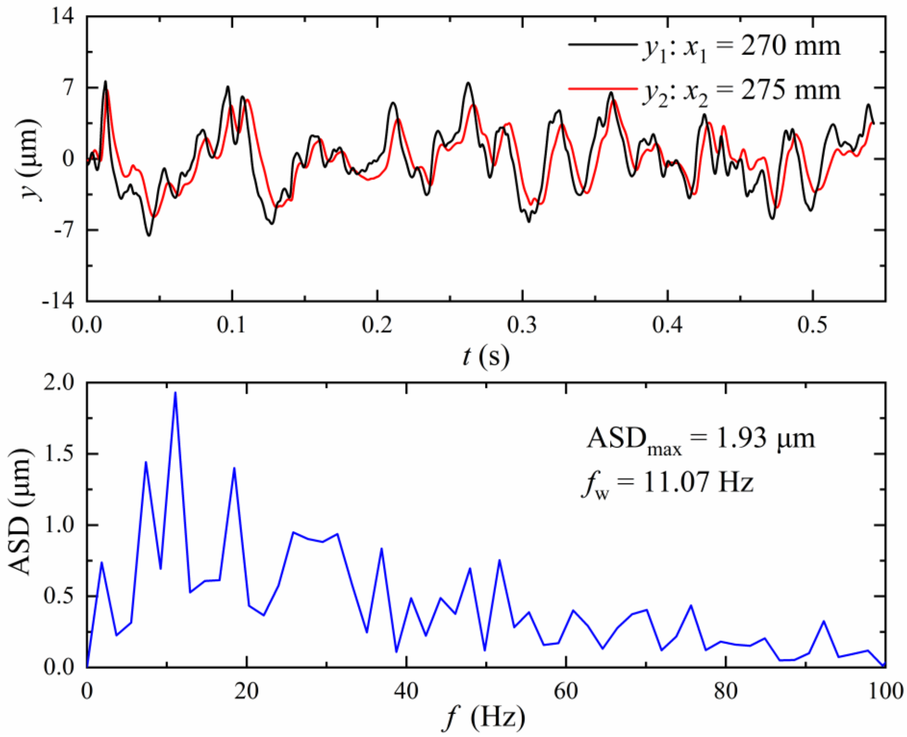

(b) Time-frequency domain diagram of the fluctuation of liquid film thickness

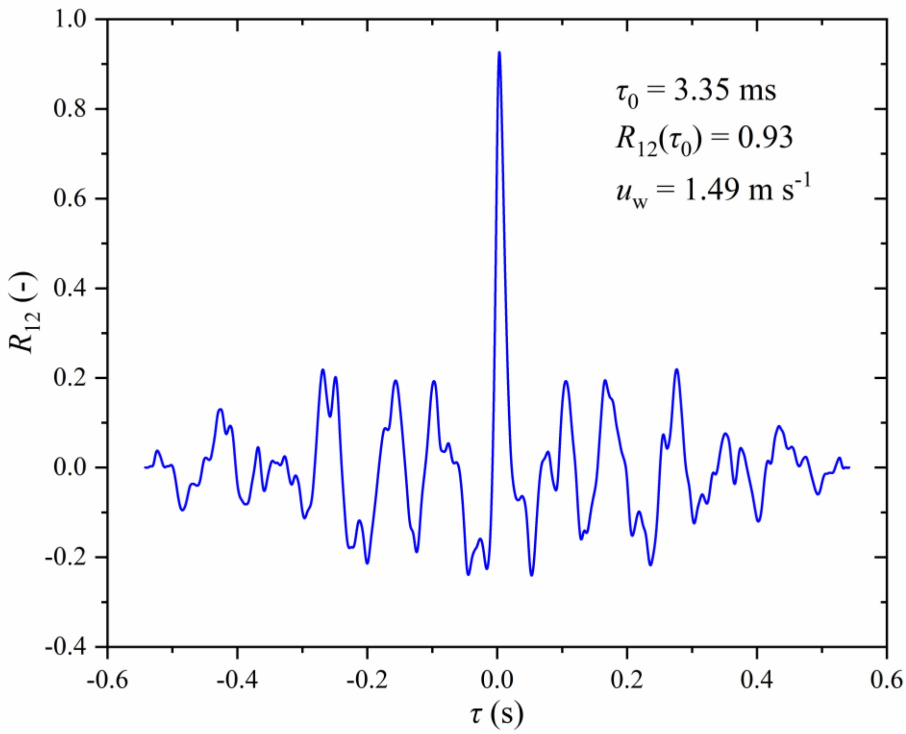

(c) Calculation of transit time using cross-correlation function

Fig. 16 The calculation process of the interfacial wave velocity (Case 4).

Table 4 Frequency and cross-correlation velocity of interfacial waves of liquid film at liquid outlet with different $\rho_{\mathrm{het}}^{\mathrm{in}}$.

Cases	δ^{wet} (μm)	f_{w} (Hz)	τ_0 (ms)	$R_{12}(\tau_0)$ (-)	u_{w} (m s^{-1})
Case 1	21	5.24	15.40	0.98	0.32
Case 2	47	7.97	9.60	0.97	0.52
Case 3	74	10.00	5.75	0.95	0.87
Case 4	89	11.07	3.35	0.93	1.49

4.3 Dehydration performance

The commonly used dehydration performance indicators are dew point depression ΔT_{d} and water removal rate η_{v} (i.e., separation efficiency). The ΔT_{d} is expressed as

$$\Delta T_{\mathrm{d}} = T_{\mathrm{d}}^{\mathrm{in}} - T_{\mathrm{d}}^{\mathrm{dry}} \tag{34}$$

where, T_{d} (°C) is the dew point temperature of gas phase. The separation efficiency η_{v} is expressed as

$$\eta_{\mathrm{v}} = \frac{\chi_{\mathrm{v}}^{\mathrm{in}} - \chi_{\mathrm{v}}^{\mathrm{dry}}}{\chi_{\mathrm{v}}^{\mathrm{in}}} \times 100\% \tag{35}$$

where, χ_{v} is the mole fraction of water vapor.

The dehydration performance of supersonic separator A is shown in Table 5. The effective water vapor partial pressure at dry gas outlet $p_{\mathrm{v}}^{\mathrm{dry}}$ includes the effective partial pressure of water vapor and liquid droplets, and its minimum value is 252.97 Pa. The dew point at dry gas outlet $T_{\mathrm{d}}^{\mathrm{dry}}$ can be as low as -10.32°C. For supersonic separator B (Case 5), $p_{\mathrm{v}}^{\mathrm{dry}}$ = 200.14 Pa, $T_{\mathrm{d}}^{\mathrm{dry}}$ = -12.93°C.

Table 5 Dehydration performance of supersonic separator A.

Cases	$p_{\mathrm{v}}^{\mathrm{dry}}$ (Pa)	$T_{\mathrm{d}}^{\mathrm{dry}}$ (°C)	$\Delta T_{\mathrm{d}}^{\mathrm{dry}}$ (°C)	η_{v} (%)
Case 1	754.63	2.93	27.07	55.58
Case 2	252.97	-10.32	40.32	85.11
Case 3	369.09	-6.01	36.01	78.27
Case 4	754.15	2.91	27.09	55.60

The histogram of the dehydration performance for different $\rho_{\mathrm{het}}^{\mathrm{in}}$ is shown in Fig. 17. It can be seen that the optimal effective density of foreign droplets $\rho_{\mathrm{het}}^{\mathrm{in}}$ is 0.01 kg m^{-3}. This means that for achieving higher dehydration efficiency, the $\rho_{\mathrm{het}}^{\mathrm{in}}$ should be moderate. If the $\rho_{\mathrm{het}}^{\mathrm{in}}$ is too small, a better swirl separation effect cannot be achieved, and more liquid droplets cannot be separated and enter the dry gas outlet, which reduces the separation efficiency. In addition, the excessive $\rho_{\mathrm{het}}^{\mathrm{in}}$ can also cause negative effects, such as thickening the liquid film against separation, increasing instability in the supersonic separator, etc. The model without considering the liquid film over-predicts the separation efficiency. When ρ_{het}^{in} = 0.01 kg m^{-3}, the maximum separation efficiency and dew point depression of separator A are 85.11% (86.71% without considering the liquid film [8]) and 40.32℃, respectively. The separation efficiency of supersonic separator B is 88.22% (93.91% without considering the liquid film [8]), and its dew point depression is 42.93℃.

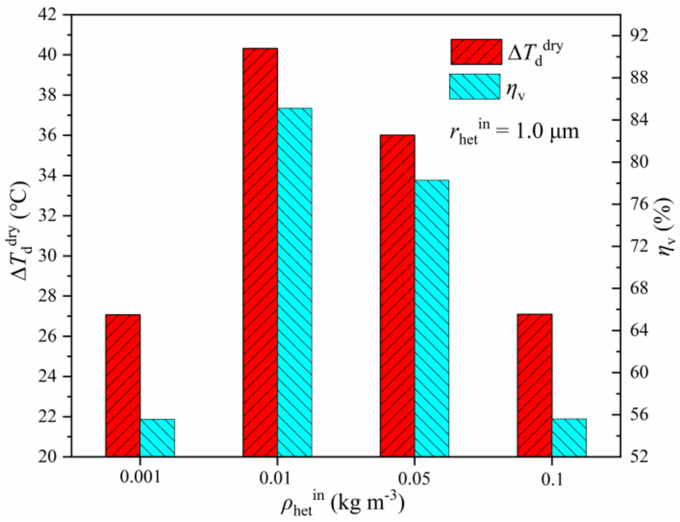

Fig. 17 Comparison of separation efficiency of different ρ_{het}^{in}.

5 Conclusion

A novel three-field two-fluid model considering the heat and mass transfer between gas, liquid droplets, and liquid film was developed and validated. Besides, the flow field, droplet behaviors, and heat transfer between the gas phase and droplets were studied. The liquid film behaviors, phase change rate, and heat flux were analyzed further. The cross-correlation algorithm was implemented to obtain the frequency and velocity of interfacial wave. Simultaneously, the effect of effective density of foreign droplets and the difference with the model without considering the liquid film was analyzed. The main conclusions are as follows:

1. The droplets start to condense at the nozzle throat but evaporate in the near-wall area and the wet gas outlet. The droplet mass change rate ranges from -283.1 kg m^{-3} s^{-1} to 412.0 kg m^{-3} s^{-1}. The maximum latent heat is 5.3×10^{8} J m^{-3} from droplets to gas phase at the condensation process, and the minimum latent heat is -3.4×10^{8} J m^{-3} at the evaporation process.

2. The slip velocity before the liquid separation position gradually increases along the flow direction, which decreases with the increase of ρ_{het}^{in}. The centrifugal velocity of the droplets is greater than that of the gas phase by a maximum of 25 m s^{-1}, so as to realize gas-liquid separation.

3. The thickness of swirling liquid film flow of Case 1-4 at wet gas outlet is 21 μm, 47 μm, 74 μm and 89 μm, respectively. At x_a = 120-220 mm, vapor phase condensation increases the liquid film mass. The

liquid film temperature decreases to a minimum 304.1 K near the axial position x_a = 120 mm due to the deposition of the dispersed droplets, where the maximum heat flux is 0.74 MW m^{-2}.

4. With the increase of ρ_{het}^{in}, the liquid film becomes thicker. Meanwhile, the frequency and velocity of the interfacial wave increase, their maximum values are 11.07 Hz and 1.49 m s^{-1} with ρ_{het}^{in} = 0.1 kg m^{-3}, which increases the instability in the separator.

5. The foreign droplets are beneficial to the dehydration performance, but it should be moderate. The optimal value of effective density of foreign droplets ρ_{het}^{in} is 0.01 kg m^{-3}. The maximum separation efficiency and dew point depression of separator A are 85.11% and 40.32℃, respectively. The model without considering the liquid film over-predicts the separation efficiency.

Acknowledgement

This work is supported in part by National Natural Science Foundation of China under Grant 51876143 and 61873184.

Data Availability Statement: The research data supporting this publication are provided within this paper.

References

[1] Khan MI, Shahrestani M, Hayat T, et al. Life cycle (well-to-wheel) energy and environmental assessment of natural gas as transportation fuel in Pakistan. Applied Energy, 2019, 242: 1738-1752.

[2] Liu Y, Cao X, Yang J, et al. Energy separation and condensation effects in pressure energy recovery process of natural gas supersonic dehydration. Energy Conversion and Management, 2021, 245: 114557.

[3] Cao X, Guo D, Sun W, et al. Supersonic separation technology for carbon dioxide and hydrogen sulfide removal from natural gas. Journal of Cleaner Production, 2021, 288: 125689.

[4] Wen C, Ding H, Yang Y. Numerical simulation of nanodroplet generation of water vapour in high-pressure supersonic flows for the potential of clean natural gas dehydration. Energy Conversion and Management, 2021, 231: 113853.

[5] Teixeira AM, de Oliveira Arinelli L, de Medeiros JL, et al. Recovery of thermodynamic hydrate inhibitors methanol, ethanol and MEG with supersonic separators in offshore natural gas processing. Journal of Natural Gas Science and Engineering, 2018, 52: 166-186.

[6] Wen C, Cao X, Yang Y, et al. Numerical simulation of natural gas flows in diffusers for supersonic separators. Energy, 2012, 37(1): 195-200.

[7] Li H, Anglart H. Prediction of dryout and post-dryout heat transfer using a two-phase CFD model. International Journal of Heat and Mass Transfer, 2016, 99: 839-850.

[8] Ding H, Sun C, Wang C, et al. Prediction of dehydration performance of supersonic separator based on a multi-fluid model with heterogeneous condensation. Applied Thermal Engineering, 2020, 171:

115074.
[9] Wang Y, Yu Y, Hu D. Experimental investigation and numerical analysis of separation performance for supersonic separator with novel drainage structure and reflux channel. Applied Thermal Engineering, 2020, 176: 115111.
[10] Wen C, Cao X, Yang Y, et al. Swirling effects on the performance of supersonic separators for natural gas separation. Chemical engineering & technology, 2011, 34(9): 1575-1580.
[11] Ma Q, Hu D, He G, et al. Performance of inner-core supersonic gas separation device with droplet enlargement method. Chinese journal of chemical engineering, 2009, 17(6): 925-933.
[12] Cao X, Yang W. The dehydration performance evaluation of a new supersonic swirling separator. Journal of Natural Gas Science and Engineering, 2015, 27: 1667-1676.
[13] Wang Y, Yu Y, Hu D. Experimental investigation and numerical analysis of separation performance for supersonic separator with novel drainage structure and reflux channel. Applied Thermal Engineering, 2020, 176: 115111.
[14] de Oliveira Arinelli L, de Medeiros JL, de Melo DC, et al. Carbon capture and high-capacity supercritical fluid processing with supersonic separator: Natural gas with ultra-high CO2 content. Journal of Natural Gas Science and Engineering, 2019, 66: 265-283.
[15] de Oliveira Arinelli L, Teixeira A M, de Medeiros J L, et al. Supersonic separator for cleaner offshore processing of natural gas with high carbon dioxide content: Environmental and economic assessments. Journal of cleaner production, 2019, 233: 510-521.
[16] Wen C, Cao X, Yang Y, et al. Evaluation of natural gas dehydration in supersonic swirling separators applying the Discrete Particle Method. Advanced powder technology, 2012, 23(2): 228-233.
[17] Yang Y, Wen C. CFD modeling of particle behavior in supersonic flows with strong swirls for gas separation. Separation and Purification Technology, 2017, 174: 22-28.
[18] Liu X, Liu Z, Li Y. Investigation on separation efficiency in supersonic separator with gas-droplet flow based on DPM approach. Separation Science and Technology, 2014, 49(17): 2603-2612.
[19] Jiang W, Bian J, Wu A, et al. Investigation of supersonic separation mechanism of CO2 in natural gas applying the Discrete Particle Method. Chemical Engineering and Processing-Process Intensification, 2018, 123: 272-279.
[20] Shooshtari SHR, Shahsavand A. Numerical investigation of water droplets trajectories during natural gas dehydration inside supersonic separator. Journal of Natural Gas Science and Engineering, 2018, 54: 131-142.
[21] Dykas S, Wróblewski W. Numerical modelling of steam condensing flow in low and high-pressure nozzles. International Journal of Heat and Mass Transfer, 2012, 55(21-22): 6191-6199.
[22] Patel Y, Patel G, Turunen-Saaresti T. Influence of turbulence modelling on non-equilibrium condensing flows in nozzle and turbine cascade. International Journal of Heat and Mass Transfer, 2015, 88: 165-180.
[23] White AJ, Hounslow MJ. Modelling droplet size distributions in polydispersed wet-steam flows. International Journal of Heat and Mass Transfer, 2000, 43(11): 1873-1884.
[24] Ding H, Tian Y, Wen C, et al. Polydispersed droplet spectrum and exergy analysis in wet steam flows

using method of moments. Applied Thermal Engineering, 2021, 182: 116148.
[25] Edathol J, Brezgin D, Aronson K, et al. Prediction of non-equilibrium homogeneous condensation in supersonic nozzle flows using Eulerian-Eulerian models. International Journal of Heat and Mass Transfer, 2020, 152: 119451.
[26] Abadi SMANR, Kouhikamali R, Atashkari K. Two-fluid model for simulation of supersonic flow of wet steam within high-pressure nozzles. International Journal of Thermal Sciences, 2015, 96: 173-182.
[27] Wen C, Karvounis N, Walther JH, et al. Non-equilibrium condensation of water vapour in supersonic flows with shock waves. International Journal of Heat and Mass Transfer, 2020, 149: 119109.
[28] Wen C, Ding H, Yang Y. Optimisation study of a supersonic separator considering nonequilibrium condensation behaviour. Energy Conversion and Management, 2020, 222: 113210.
[29] Niknam PH, Mortaheb HR, Mokhtarani B. Dehydration of low-pressure gas using supersonic separation: Experimental investigation and CFD analysis. Journal of Natural Gas Science and Engineering, 2018, 52: 202-214.
[30] Shooshtari SHR, Shahsavand A. Optimal operation of refrigeration oriented supersonic separators for natural gas dehydration via heterogeneous condensation. Applied Thermal Engineering, 2018, 139: 76-86.
[31] Deng Y, Zhang L, Hou H, et al. Modeling and simulation of the gas-liquid separation process in an axial flow cyclone based on the Eulerian-Lagrangian approach and surface film model. Powder Technology, 2019, 353: 473-488.
[32] Han J, Feng J, Hou T, et al. Numerical and experimental study on gas-water separators for a PEMFC system. International Journal of Green Energy, 2021, 18(5): 490-502.
[33] Li H, Anglart H. Prediction of dryout and post-dryout heat transfer using a two-phase CFD model. International Journal of Heat and Mass Transfer, 2016, 99: 839-850.
[34] Yue T, Chen J, Song J, et al. Experimental and numerical study of upper swirling liquid film (USLF) among gas-liquid cylindrical cyclones (GLCC). Chemical Engineering Journal, 2019, 358: 806-820.
[35] Kantrowitz A. Nucleation in very rapid vapor expansions. The Journal of chemical physics, 1951, 19(9): 1097-1100.
[36] Jurski K, Géhin E. Heterogeneous condensation process in an air water vapour expansion through a nozzle—experimental aspect. International journal of multiphase flow, 2003, 29(7): 1137-1152.
[37] O'Rourke PJ. Collective Drop Effects on Vaporizing Liquid Sprays. PhD thesis. Princeton University, Princeton, New Jersey. 1981.
[38] Ounis H, Ahmadi G, McLaughlin J B. Brownian diffusion of submicrometer particles in the viscous sublayer. Journal of Colloid and Interface Science, 1991, 143(1): 266-277.
[39] Wang B, Xu D, Chu K, et al. Numerical study of gas-solid flow in a cyclone separator. Applied Mathematical Modelling, 2006, 30(11): 1326-1342.
[40] Dykas S, Wróblewski W. Two-fluid model for prediction of wet steam transonic flow. International Journal of Heat and Mass Transfer, 2013, 60: 88-94.
[41] Yuan S, Fan Y, Chen B, et al. Forming and stripping of the wall film and the influence on gas-liquid separation. Asia-Pacific Journal of Chemical Engineering. 2020, 15(3): e2447.

[42] Wang X, Chang H, Corradini M, et al. Prediction of falling film evaporation on the AP1000 passive containment cooling system using ANSYS FLUENT code. Annals of Nuclear Energy. 2016, 95: 168-175.
[43] Baker N, O'Sullivan P. Verification of Multiphase Flow CFD Simulation and Grid Convergence Index (GCI) Analysis, 2013.
[44] Wang B, Xu D L, Chu K W, et al. Numerical study of gas-solid flow in a cyclone separator. Applied Mathematical Modelling, 2006, 30(11): 1326-1342.
[45] Du K, Hu P, Hu Z. Numerical Investigation of Water Film Evaporation with the Countercurrent Air in the Asymmetric Heating Rectangular Channel for Passive Containment Cooling System. Science and Technology of Nuclear Installations, 2020.
[46] Wang C, Zhao N, Feng Y, et al. Interfacial wave velocity of vertical gas-liquid annular flow at different system pressures. Experimental Thermal and Fluid Science, 2018, 92: 20-32.